Journal of Computational Physics 415 (2020) 109510

Contents lists available at ScienceDirect

Journal of Computational Physics

www.elsevier.com/locate/jcp

Exact and locally implicit source term solvers for multifluid-Maxwell systems

Liang Wang [a,b,*], Ammar H. Hakim [b], Jonathan Ng [c,a,b,d], Chuanfei Dong [a,b], Kai Germaschewski [e]

[a] Princeton University, Princeton, NJ, 08544, United States of America
[b] Princeton Plasma Physics Laboratory, Princeton, NJ 08543, United States of America
[c] University of Maryland, College Park, College Park, MD 20742, United States of America
[d] NASA Goddard Space Flight Center, Greenbelt, MD 20771, United States of America
[e] Space Science Center, University of New Hampshire, Durham, NH 03824, United States of America

ARTICLE INFO

Article history:
Received 10 October 2019
Received in revised form 10 April 2020
Accepted 27 April 2020
Available online 6 May 2020

Keywords:
Multifluid plasma model
Implicit source term
Five-moment
Ten-moment

ABSTRACT

Recently, a family of models that couple multifluid systems to the full Maxwell equations have been used in laboratory, space, and astrophysical plasma modeling. These models are more complete descriptions of the plasma than reduced models like magnetohydrodynamic (MHD) since they are derived more closely from the full kinetic Vlasov-Maxwell system, without assumptions like quasi-neutrality, negligible electron mass, etc. Thus these models naturally retain non-ideal MHD effects like electron inertia, Hall term, pressure anisotropy/nongyrotropy, displacement current, among others. One obstacle to broader application of these models is that an explicit treatment of their source terms leads to the need to resolve rapid processes like plasma oscillation and electron cyclotron motion, even when these are not important. In this paper, we suggest two ways to address this issue. First, we derive the analytic solutions to the source update equations, which can be implemented as a practical, but less generic solver. We then develop a time-centered, locally implicit algorithm to update the source terms, allowing stepping over the fast kinetic time-scales. For a plasma with S species, the locally implicit algorithm involves inverting a local $(3S+3)\times(3S+3)$ matrix only, thus is very efficient. The performance can be further increased by using the direct update formulas to skip null calculations. We present benchmarks illustrating the exact energy-conservation of the locally implicit solver, as well as its efficiency and robustness for both small-scale, idealized problems and large-scale, complex systems. The locally implicit algorithm can be also easily extended to include other local sources, like collisions and ionization, which are difficult to solve analytically.

* Corresponding author at: Princeton Plasma Physics Laboratory, Princeton, NJ 08543, United States of America.
E-mail address: lwang@pppl.gov (L. Wang).

https://doi.org/10.1016/j.jcp.2020.109510
0021-9991/

1. Introduction

In this paper we describe numerical methods to update source terms for the multifluid plasma equations coupled to Maxwell equations. These models consist of equations of velocity moments for each plasma species s, in the conservative form,

$$\frac{\partial_t (m_s n_s)}{\partial t} + \frac{\partial \left(m_s n_s u_{j,s}\right)}{\partial x_j} = 0 \tag{1}$$

$$\frac{\partial \left(m_s n_s u_{j,s}\right)}{\partial t} + \frac{\partial \mathcal{P}_{ij,s}}{\partial x_j} = n_s q_s \left(E_i + \epsilon_{ijk} u_{j,s} B_k\right) \tag{2}$$

Here, q_s and m_s are the particle charge and mass, ε_{ijk} is the Levi-Civita symbol. The moments are defined as

$$n_s(\mathbf{x}) \equiv \int f_s d\mathbf{v} \tag{3}$$

$$m_s n_s(\mathbf{x}) u_{i,s}(\mathbf{x}) \equiv m_s \int v_i f_s d\mathbf{v} \tag{4}$$

$$\mathcal{P}_{ij,s}(\mathbf{x}) \equiv m_s \int v_i v_j f_s d\mathbf{v} \tag{5}$$

with $f_s(\mathbf{x}, \mathbf{v}, t)$ being the phase space distribution function. We will neglect the subscript s hereinafter for convenience. For completeness, $\mathcal{P}_{ij}$ relates to the more familiar thermal pressure tensor

$$P_{ij} \equiv m \int (v_i - u_i)\left(v_j - u_j\right) f d\mathbf{v} \tag{6}$$

by

$$\mathcal{P}_{ij} = P_{ij} + nmu_i u_j. \tag{7}$$

For simplicity, non-ideal effects like viscous dissipation are neglected. The electric and magnetic fields $\mathbf{E}$ and $\mathbf{B}$ are evolved using Maxwell equations

$$\frac{\partial \mathbf{B}}{\partial t} + \nabla \times \mathbf{E} = 0 \tag{8}$$

$$\frac{\partial \mathbf{E}}{\partial t} - c^2 \nabla \times \mathbf{B} = -\frac{1}{\varepsilon_0} \sum_s q_s n_s \mathbf{u}_s \tag{9}$$

with $c = 1/\sqrt{\mu_0 \varepsilon_0}$ being the speed of light.

To close the system, the second order moment $\mathcal{P}_{ij}$ or P_{ij} must be specified. For example, a cold fluid closure simply sets $P_{ij} = 0$, while an isothermal equation of state (EOS) assumes that the temperature is constant. Or, assuming zero heat flux and that the pressure tensor is isotropic, we can write an adiabatic EOS for $P_{ij} = p\mathcal{I}$

$$\frac{\partial \mathcal{E}}{\partial t} + \nabla \cdot [(p + \mathcal{E})\mathbf{u}] = nq\mathbf{u} \cdot \mathbf{E}, \tag{10}$$

where

$$\mathcal{E} \equiv \frac{p}{\gamma - 1} + \frac{1}{2}\rho |\mathbf{u}|^2 \tag{11}$$

is the total fluid (thermal plus kinetic) energy and γ is the adiabatic index, set to 5/3 for a fully ionized plasma. For a plasma with S species ($s = 1, \ldots, S$) this system is closed and has a total of $5S + 6$ equations, and are here referred to as the FIVE-MOMENT model [1]. More general models can be obtained by retaining the evolution equations for all six components of the pressure tensor [2,3] in the so-called TEN-MOMENT model

$$\frac{\partial \mathcal{P}_{ij,s}}{\partial t} + \frac{\partial \mathcal{Q}_{ijm,s}}{\partial x_m} = n_s q_s u_{[i,s} E_{j]} + \frac{q_s}{m_s} \epsilon_{[iml} \mathcal{P}_{mj],s} B_l \tag{12}$$

where the third moment

$$\mathcal{Q}_{ijm,s}(\mathbf{x}) \equiv m_s \int v_i v_j v_m f_s d\mathbf{v} \tag{13}$$

relates to the heat flux tensor defined in the fluid frame

$$Q_{ijm} \equiv m \int (v_i - u_i)(v_j - u_j)(v_m - u_m) f d\mathbf{v} \tag{14}$$

by

$$\mathcal{Q}_{ijm} = Q_{ijm} + u_{[i}\mathcal{P}_{jm]} - 2nmu_i u_j u_m. \tag{15}$$

Again, the equations here must be closed by some approximation for the heat-flux tensor [4,5]. Another option is to include evolution equations for even higher order moments, e.g., the ten independent components of the heat-flux tensor [6].

Theoretically, the multifluid-Maxwell equations approach the Hall magnetohydrodynamics (MHD) under asymptotic limits of vanishing electron mass and infinite speed of light, as demonstrated in great detail by Refs. [7,8,4,9]. All waves and effects within the two-fluid picture are retained, for example, the light wave, electron and ion inertial effects like the ion cyclotron wave and whistler wave. Particularly, through properly devised heat-flux closures, the ten-moment model could partially capture nonlocal kinetic effects like Landau damping, in a manner similar to the gyrofluid models [10,5,11,12].

Although multifluid-Maxwell models provide a more complete description of the plasma than reduced, asymptotic models like MHD [8,4], they are less frequently used. The reason for this is the fast kinetic scales involved. Retaining the electron inertia adds plasma-frequency and cyclotron time-scale, while non-neutrality adds Debye length spatial-scales. Further, inclusion of the displacement currents means that electromagnetic (EM) waves must be resolved when using an explicit scheme. Fortunately, the restrictions due to kinetic scales are introduced only through the non-hyperbolic source terms of Eqns. (2), (9), and Eqn. (12). Therefore we may eliminate these restrictions by updating the source term separately either exactly or using an implicit algorithm. This allows larger time steps and leads to significant speedup, especially with realistic electron/ion mass ratios. Developing such source term update schemes is the focus of this paper. The speed of light constraint still exists, however, can be greatly relaxed, using reduced values for the speed of light and/or sub-cycling Maxwell equations. Of course, an implicit Maxwell solver, or a reduced set of electromagnetic equations like the Darwin approximation [13], can also relax the time-step restrictions. In either case, though, a fully implicit approach is needed, which is not considered in this paper.

The rest of the paper is organized as follows. First, the source term update equations are written down as time-dependent constant-coefficient ordinary differential equations (ODEs). We then briefly discuss the availability of exact solutions for the source update equations, but subsequently focused on a more efficient and versatile locally implicit algorithm. It is shown that the time-steps are restricted solely by the speed of light, and that the algorithm preserves positivity of density and pressure. The accuracy and robustness of both (i.e., the analytic solution and the locally implicit solution) methods are demonstrated through a few standard benchmark problems, as well as through an application to large-scale modeling of the interaction between solar wind and Earth's magnetosphere. The appendix gives a thorough derivation of the exact solutions plus direct formulae for the locally implicit schemes. The eigensystem of the ten-moment model, useful for implementing approximate Riemann solvers for this system, is provided in the appendix too.

2. An operator splitting scheme and the source term update equations

The multifluid-Maxwell equations can be split into a homogeneous part and a source term update part. The key idea is to solve these two parts separately and apply high accuracy schemes on both.

Ignoring sources, the *homogeneous* equations can be solved in the *conservation law form*

$$\frac{\partial \mathbf{Q}}{\partial t} + \nabla \cdot \mathbf{F} = 0 \tag{16}$$

where $\mathbf{Q}$ is the vector of conserved quantities (fluid moments and electromagnetic field) and $\mathbf{F}$ are the corresponding fluxes. See Eqns. (1)–(3) of [1] for the conservation form of five-moment equations, and Eqns. (24)–(25) of [2] for the conservation form of the ten-moment equations. An explicit solution of Eqn. (16) is subject to light speed constraint $c\Delta t/\Delta x < \text{CFL}$, where Δx is the (smallest) grid spacing and $\text{CFL} \leq 1$ is determined from the spatial scheme used. The often more restrictive constraints due to kinetic scales are contained in the remaining non-hyperbolic, source term update part only. This implies that it is possible to eliminate these constraints if a proper implicit algorithm is applied to update the source term.

Deferring the source term details to the next paragraph, we represent the *homogeneous* update schematically as the operator $\exp(\mathcal{L}_H \Delta t)$ and the *source* update as $\exp(\mathcal{L}_S \Delta t)$. The full algorithm can now be written as the Strang-splitting sequence that has second order accuracy in time [14],

$$\exp(\mathcal{L}_S \Delta t/2) \exp(\mathcal{L}_H \Delta t) \exp(\mathcal{L}_S \Delta t/2). \tag{17}$$

The remainder of this paper is devoted to developing schemes for $\exp(\mathcal{L}_S \Delta t)$. As for $\exp(\mathcal{L}_H \Delta t)$, one can use a number of schemes, including the finite-volume (FV) wave-propagation scheme [15,1], a variation of the MUSCL algorithm [16], or a discontinuous Galerkin (DG) scheme [17–19], among others. Each of these schemes has advantages: finite-volume methods are robust and easy to implement, while DG schemes are high-order and have the potential of providing higher accuracy at a lower cost compared to second-order schemes.

Now we consider the source update equations. For the five-moment model, the source terms are

$$\begin{cases} \left(\frac{\partial \mathbf{J}_s}{\partial t}\right)_{\text{source}} & = \omega_s^2 \varepsilon_0 \mathbf{E} + \mathbf{J}_s \times \mathbf{\Omega}_s \\ \varepsilon_0 \left(\frac{\partial \mathbf{E}}{\partial t}\right)_{\text{source}} & = -\sum_s \mathbf{J}_s. \end{cases} \tag{18}$$

Here, $\mathbf{\Omega}_s \equiv q_s \mathbf{B}/m_s$ is the cyclotron frequency, $\omega_s \equiv \sqrt{q_s^2 n_s/\varepsilon_0 m_s}$ is the species plasma frequency, and we use currents, $\mathbf{J}_s \equiv q_s n_s \mathbf{u}_s$, instead of momentum for convenience. The subscript "source" means that update equations are for the source terms, separate from the hyperbolic part. In the rest of the paper, these subscripts will be ignored for simplicity. During the source term update, the plasma density n_s and magnetic field $\mathbf{B}$ remain unchanged and this coupled system has an energy invariant,

$$\sum_s \frac{1}{2} \frac{\mathbf{J}_s^2}{\varepsilon_0 \omega_s^2} + \frac{\varepsilon_0}{2} \mathbf{E}^2 = \text{const.} \tag{19}$$

It should be noted that, superficially, one needs to solve the source term for the scalar energy equation. However, this source term only allows energy transfer between the plasma and the electric field and does not alter the plasma pressure. Therefore, we may accumulate changes in the bulk kinetic energy to update the total internal energy. This avoids truncation errors that might lead to negative plasma pressure if we solve the scalar energy source term equation.

The ten-moment model has the same source terms for currents and the electric field. In addition, there are source terms in the pressure tensor equation (12) that accounts for a rotation around the background magnetic field

$$\frac{\partial \mathbf{P}_s}{\partial t} = \text{Sym2}\left(\mathbf{P}_s \times \mathbf{\Omega}_s\right). \tag{20}$$

Here, $\text{Sym2}\left(\mathbf{V}\right)$ denotes the space of all symmetric tensors of 2nd order defined on the tensor $\mathbf{V}$.

3. A locally implicit scheme

3.1. Availability of exact solutions

During the source term updates Eqn. (18) and (B.16), the plasma densities and magnetic field remain unchanged. Consequently, the equations are effectively constant-coefficient linear ODEs in time. They can be solved exactly to obtain currents/electric field or pressure tensor as functions of time. Ref. [3] obtained such exact, analytic solutions in the simplified two-fluid case. After tedious algebraic derivations, we can unify and generalize this procedure for any number of species. The derivations and resulting algorithms can be found in Appendix B.

3.2. The locally implicit scheme

The exact solution algorithm is very complex, though feasible, and relatively expensive, thus it is not optimal for large-scale simulations. In this section, we propose to use a locally implicit scheme that is more efficient. In this section, we present a *locally implicit* scheme to update the source term equations more efficiently using a centered discretization in time. Using this scheme, it is also straightforward to include additional source terms that depend on local quantities only, e.g., collisions and ionization. It is worthwhile to mention that schemes using implicit–explicit (IMEX) timestepping to treat the source terms are described in [20–22]. A more recent work coupled a biased implicit treatment of the source term in with the hyperbolic update [23]. However the scheme presented here is considerably simpler as we work with the non-conservative form of the equations *just for the source updates*. In any case, the scheme in [20] is implicitly contained in earlier two-fluid papers [24,1], which essentially only performed a single (or few) iteration(s) of the implicit scheme in [20]. Note that this our algorithm is inspired by [25] that used a similar approach to solve the Lorentz and Ampere update equations for current $\mathbf{J_s}$ of each plasma species and electric field $\mathbf{E}$. The major difference is that we have incorporated the Lorentz-Ampere update equations into the full multifluid-Maxwell system and significantly broadened the scope of applications. In addition, we present a more complete analysis of the algorithm along with broader application examples.

3.3. The scheme

For numerical stability, it is intuitive to apply the backward Euler method,

$$\begin{cases} \mathbf{J}_s^{n+1} & = \mathbf{J}_s^n + \frac{\Delta t}{2}\left(\omega_s^2 \varepsilon_0 \mathbf{E}^{n+1} + \mathbf{J}_s^{n+1} \times \mathbf{\Omega}_s\right) \\ \mathbf{E}^{n+1} & = \mathbf{E}^n - \frac{\Delta t}{2\varepsilon_0} \sum_s \bar{\mathbf{J}}_s \end{cases} \tag{21}$$

which was adopted by [21]. However, this is a first order method and damps the oscillatory solutions. A slight modification improves both stability and energy conservation. For convenience, we introduce time-centered quantities

$$\bar{\mathbf{J}}_s \equiv (\mathbf{J}_s^{n+1} + \mathbf{J}_s^n)/2 \quad \text{and} \quad \bar{\mathbf{E}} \equiv (\mathbf{E}^{n+1} + \mathbf{E}^n)/2 \tag{22}$$

The first part of our scheme is given by

$$\begin{cases} \bar{\mathbf{J}}_s &= \mathbf{J}_s^n + \frac{\Delta t}{2}\left(\omega_s^2 \varepsilon_0 \bar{\mathbf{E}} + \bar{\mathbf{J}}_s \times \boldsymbol{\Omega}_s\right) \\ \bar{\mathbf{E}} &= \mathbf{E}^n - \frac{\Delta t}{2\varepsilon_0} \sum_s \bar{\mathbf{J}}_s \end{cases} \tag{23}$$

and can be rearranged into the form

$$\begin{cases} \bar{\mathbf{J}}_s - \frac{\Delta t}{2}\left(\omega_s^2 \varepsilon_0 \bar{\mathbf{E}} + \bar{\mathbf{J}}_s \times \boldsymbol{\Omega}_s\right) &= \mathbf{J}_s^n \\ \bar{\mathbf{E}} + \frac{\Delta t}{2\varepsilon_0} \sum_s \bar{\mathbf{J}}_s &= \mathbf{E}^n \end{cases} \Leftrightarrow \mathbf{M}_{l.h.s.} \begin{bmatrix} \bar{\mathbf{J}}_s \\ \bar{\mathbf{E}} \end{bmatrix} = \begin{bmatrix} \mathbf{J}_s \\ \mathbf{E} \end{bmatrix} \tag{24}$$

with $\mathbf{M}_{l.h.s.}$ being the $(3S+3) \times (3S+3)$ constant coefficient matrix.

Eqn. (24) is a system of linear, constant-coefficient ODEs for the $3S+3$ unknowns $\bar{\mathbf{J}}_s$ and $\bar{\mathbf{E}}$ and can be solved with any linear algebra routine to get

$$\begin{bmatrix} \bar{\mathbf{J}}_s \\ \bar{\mathbf{E}} \end{bmatrix} = \mathbf{M}_{l.h.s.}^{-1} \begin{bmatrix} \mathbf{J}_s \\ \mathbf{E} \end{bmatrix}. \tag{25}$$

The final updated currents and electric field can then be determined by

$$\mathbf{E}^{n+1} = 2\bar{\mathbf{E}} - \mathbf{E}^n \quad \text{and} \quad \mathbf{J}_s^{n+1} = 2\bar{\mathbf{J}}_s - \mathbf{J}_s^n. \tag{26}$$

We call this scheme the locally implicit scheme as it involves only data in a single cell and requires the inversion of only a $(3S+3)^2$ matrix. No global matrix inversion coupling all cells in the domain is required. If a DG scheme is used, then the source update needs to be computed at each node of the selected finite-element node, or, projected onto the selected modal basis, if using those. In Appendix D, inspired by [25], we show that it is also possible to write down the resultant formulae for the complete linear algebra calculations and skip the "null" calculations (e.g., zeros multiplied by zeros) for significant speedup.

3.4. Accuracy and stability

Indeed, the locally implicit scheme is an implicit midpoint method, giving an error of order $O\left((\Delta t)^2\right)$. The stability of the algorithm can be studied by a von Neumann analysis. We introduce a time-dependence of $e^{-i\omega t}$, where ω is the (possibly complex) numerical frequency. For plasma oscillations the source update has the numerical dispersion relation (see Section. E)

$$4/\Delta t^2 \tan^2(\omega \Delta t/2) = \omega_p^2 \tag{27}$$

showing that the time-step is not restricted by plasma frequency. In a similar way, we can show that the time step is not restricted by cyclotron frequency, either.

3.5. Conservation properties

To ensure that the number density and pressure remain positive, we first observe that the source update Eqns. (30) do not modify either of these quantities. Hence, positivity violations can only occur in the homogeneous updates of the fluid quantities.

The multifluid system, in the absence of dissipation and with appropriate boundary conditions,[1] conserves the total energy, i.e. $d\mathcal{E}/dt = 0$, where

$$\mathcal{E} = \int \left[\sum_s \left(\frac{1}{2} m_s \mathbf{u}_s^2 + \frac{3}{2} p_s \right) + \frac{\epsilon_0}{2} \mathbf{E}^2 + \frac{1}{2\mu_0} \mathbf{B}^2 \right] d\mathbf{x} \tag{28}$$

and the integration is taken over the whole domain. The source update, Eqns. (23) as can be shown easily, conserve the discrete form of Eqn. (19). This can be further understood as the merit of the implicit midpoint method that it preserves the magnitude of any oscillatory systems. Also, solving the homogeneous fluid equation in conservation law form conserves the fluid energies. Hence, the conservation of the total discrete energy, including electromagnetic energy, depends on the scheme selected to solve Maxwell equations. In general, upwind finite-volume schemes will *not* conserve the EM energy,

[1] Energy conservation for *homogeneous* fluid equations is exact for periodic boundaries. However, for wall boundary small energy errors arise due to diffusive terms in the numerical fluxes used. One can always use a central flux at walls, but this complicates the scheme, and is not always worth the effort in practice.

but *decay* it. Hence, unless an energy conserving finite-volume/difference scheme is used to update the EM fields, the total energy is not conserved by the discrete scheme. Even when using an upwind scheme, lack of energy conservation is not always a problem, however, as the energy conservation error scales as the order of the scheme, and hence can be controlled by using a finer mesh or a higher order method.

3.6. Including collisions

Following [25], we may incorporate frictional collisions by slightly modifying the current source term as

$$\left(\frac{\partial}{\partial t} + \nu_s\right)\mathbf{J}_s = \omega_s^2 \varepsilon_0 \mathbf{E} + \mathbf{J}_s \times \mathbf{\Omega}_s \tag{29}$$

where ν_s is a constant collision frequency. The additional collision term converts the solution from purely oscillatory to damped oscillations. The corresponding locally implicit scheme is written as

$$\begin{cases} \bar{\mathbf{J}}_s & = \mathbf{J}_s^n + \frac{\Delta t}{2}\left(\omega_s^2 \varepsilon_0 \bar{\mathbf{E}} + \bar{\mathbf{J}}_s \times \mathbf{\Omega}_s - \nu_s \bar{\mathbf{J}}_s\right) \\ \bar{\mathbf{E}} & = \mathbf{E}^n - \frac{\Delta t}{2\varepsilon_0}\sum_s \bar{\mathbf{J}}_s. \end{cases} \tag{30}$$

This is still a constant coefficient linear system, thus can also be solved using any linear algebra routine. In a similar manner, we may include additional source terms, e.g., ionization, gravity, chemical production, as long as the terms involves only local quantities (i.e., no gradient calculations etc.).

4. Benchmark problems

In this section, we present a few benchmark simulations to illustrate the properties of the locally implicit scheme. In all but the first test, we use a dimensionally split version of the FV discretization described in [1]. Note that the purpose of the paper is not to study the *detailed physics* of these problems, but to simply show that the algorithm presented above is efficient and stable where the explicit algorithm would be unstable, and produces qualitatively correct results.

4.1. Plasma oscillation

As our first benchmark, we consider the plasma oscillation of one species locally, i.e., within a cell. In other word, we disregard the spatial integration Eqn. (16) and integrates only Eqn. (18). The purpose is to verify the conservation property of the time-centered scheme. The initial condition consists of a uniform, stationary plasma and vanishing magnetic field. Perturbation is imposed on E_x. Therefore the initial condition is an eigenvector of $\omega = \omega_p$ (see the exact solution Eqn. (B.8)). The ions are assumed to be immobile. We performed three simulations as presented in the three columns in Fig. 1. The upper and lower rows are the time evolution of E_x and the phase-diagram for the normalized electric field $\tilde{E}_x$ and current $\tilde{J}_{x,e}$ (see Eqn. (B.3)), respectively. Ideally, the system should oscillate at the plasma frequency ω_{pe} and the total normalized energy $\tilde{E}_x^2 + \tilde{J}_{x,e}^2$ should remain constant following energy conservation.

The simulation in the left column uses the first-order backward-Euler implicit algorithm. Even with a small time step $\Delta t = 0.1/\omega_{pe}$, the solution is quickly damped. In comparison, the middle-column simulation that uses the time-centered implicit algorithm is able to model the oscillation at the correct frequency and does not suffer from any damping. The conservation property of the time-centered algorithm can be further confirmed from the right-column run that uses a large time step $\Delta t = 10000/\omega_{pe}$ with the time-centered algorithm (see the lower panel). At such a large time step, however, the plasma oscillation are aliased by slower oscillations that are supported by the time step size.

4.2. Plasma wave-beach

We now show a few more practical problems that couple the homogeneous part and the source term part. The first is a "plasma wave-beach" problem, in which power is propagated in a 1 m long hydrogen plasma of increasing density, such that the wave suffers a cutoff at $x = 0.58$ m. Letting $\delta t = 1/100c$, the plasma profile is $\omega_e(x)\delta t = (1-x)^5$. For the 100 cell simulation shown in Fig. 2, hence, the time-step, restricted only by the CFL condition, is $\omega_e \Delta t = 25$, 12.5 times larger than would be allowed by a fully explicit scheme, which has a restriction $\omega_e \Delta t < 2$.

4.3. Magnetic reconnection in a Harris current sheet

The second simulation is of magnetic reconnection in a Harris current sheet. For this, the standard GEM reconnection challenge parameters are used [26], with an initial equilibrium magnetic field $B_x(y) = B_0 \tanh(y/L)$, supported by a out-of-plane current sheet with both electrons and ions carrying current. The simulation parameters are

$$\frac{\lambda}{d_i} = 0.5,\ \frac{m_i}{m_e} = 100,\ \frac{T_i}{T_e} = 5,\ \frac{n_b}{n_0} = 0.2,\ \frac{V_{A0}}{c} = 0.05 \tag{31}$$

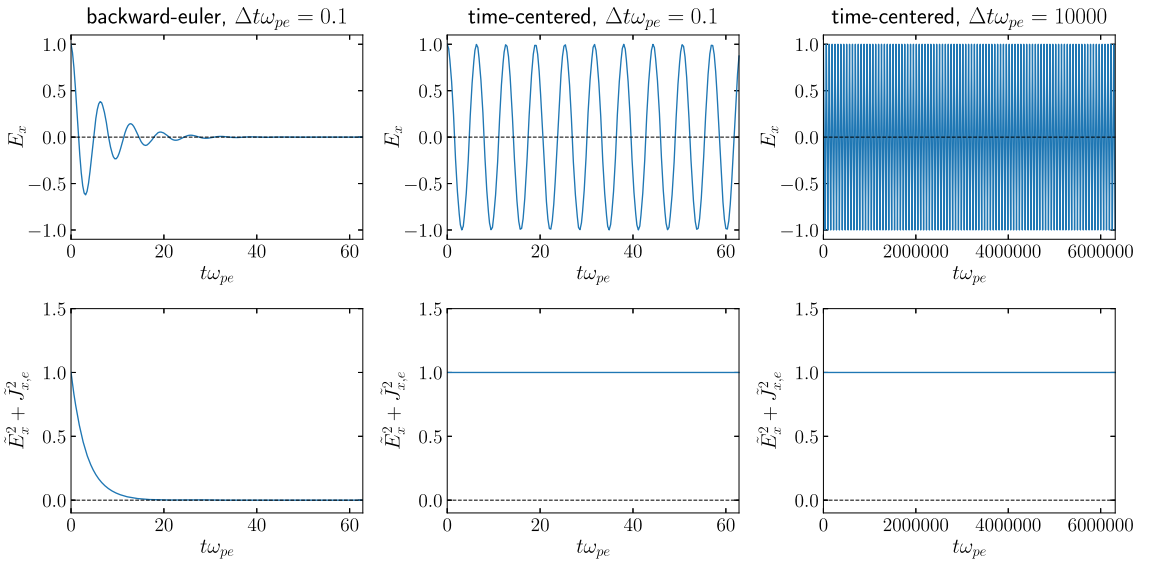

Fig. 1. Electron plasma oscillation using the first-order backward Euler scheme (left column) and locally implicit time-centered algorithm (middle and right columns). *Upper row*: Temporal evolution of E_x. *Lower row*: Temporal evolution of total normalized energy $\tilde{E}_x^2 + \tilde{J}_{x,e}^2$. The time-centered simulations are fully oscillatory without any damping or instability.

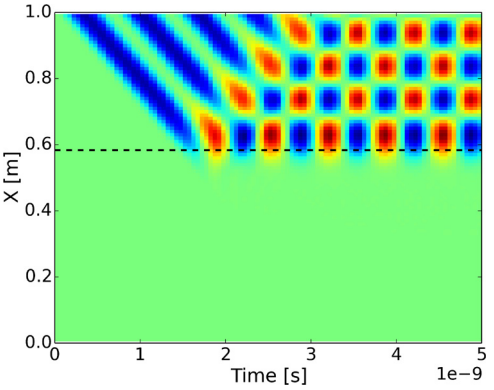

Fig. 2. Propagation of an electromagnetic (EM) wave into a "plasma wave-beach". Shown are contours of the y-component of the electric field, time increasing from left to right. The EM wave is launched by applying a current (J_y) at $x = 1$, with frequency $\omega\delta t = \pi/10$, with $\delta t = 1/100c$. The wave suffers a cutoff (black dashed line), reflecting back into the low-density region, creating a standing wave pattern late in time. The time-step is 12.5× larger than for a fully explicit scheme, which would have a restriction $\omega_e \Delta t < 2$.

where $d_i = c/\omega_{pi}$ is the ion inertial length, T_i and T_e are the ion and electron temperatures, and $v_{A0} = B_0/\sqrt{\mu_0 n_0 m_i}$ is the Alfvén velocity. The plasma beta is unity. A grid of 64×32 cells was used, with a CFL number of 0.9, resulting in a time-step of $\omega_{pe}\Delta t \approx 3.6$. The cell spacing is about 27× larger than the Debye length. The results are summarized in Fig. 3. Even on this coarse mesh, with the plasma frequency unresolved and the Debye length severely under-resolved, the algorithm is stable and produces results qualitatively similar to higher resolution results published in [1,19]. In detail, the left panel of Fig. 3 clearly shows the reconnected electron current sheet structure. The middle panel shows the quadrupolar out-of-plane magnetic field formed due to Hall currents, which would be vanishing in an MHD simulation where the Hall effect is missing. The right panel shows the dissipation regions marked by nonvanishing $\mathbf{J} \cdot \mathbf{E}$, which is intensified at the X-point and in the outflow exhaust, in agreement with prior fully kinetic studies. More thorough studies of magnetic reconnection in the context of Earth's magnetosphere, etc. can be found in [27] and [4].

4.4. Orszag-Tang vortex

The fourth test is five-moment simulation of the Orszag-Tang vortex [28], a 2D problem extensively used to benchmark and compare numerical codes [29–31]. We use a $[0, 2\pi] \times [0, 2\pi]$ periodic domain on a 128×128 grid. The initial condition consists of uniform total mass density $\rho = 25/9$, uniform total pressure $p = 5/3$, in-plane flow vortex $v_x = -\sin y$, $v_y = \sin x$, and magnetic field vortex $B_x = -\sin y$, $B_y = \sin(2x)$. The ion charge/mass ratio is so that the ion inertia lengths based

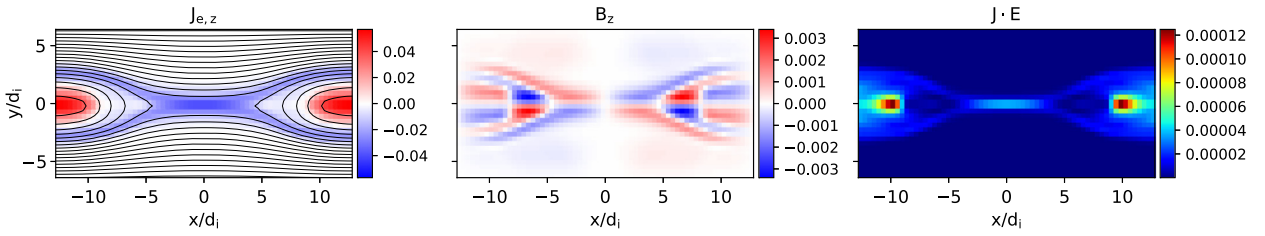

Fig. 3. Results from the 2D GEM reconnection simulation that is severely under-resolved but remains stable. *Left*: Out-of-plane electron current and contours of in-plane magnetic field. *Middle*: Out-of-plane magnetic field. *Right*: $\mathbf{J}\cdot\mathbf{E}$ dissipation.

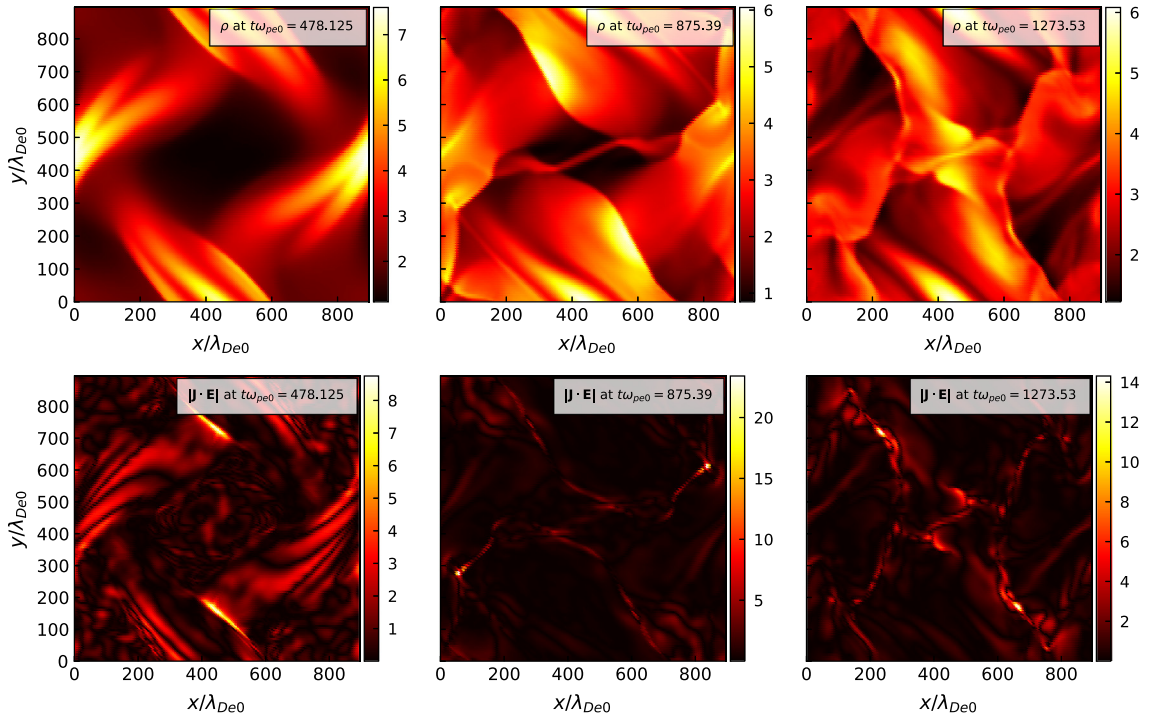

Fig. 4. Total mass densities (i.e., electron plus ion mass densities*upper row*) and $\mathbf{J}\cdot\mathbf{E}$ dissipation (*lower row*) at different stages (*different columns*) in the five-moment Orszag-Tang vortex test. The simulation is performed on a low-resolution 128^2 grid, with Δx about $7\times$ the electron Debye length λ_{De0}. Structures like shocks and current sheets are correctly captured.

on initial background density is $d_i = \sqrt{\rho_i q_i^2/\varepsilon_0 m_i^2} = 2\pi/25$. Other parameters include $\gamma = 5/3$, $\mu_0 = 1$, $c = 20$, $m_i/m_e = 25$, and $p_i/p_e = 1$. As shown in the upper row of Fig. 4, the formation of shocks and thin current layer at the center is clearly captured. The lower panel of Fig. 4 shows at different stages the dissipation develops in localized layers at the shocks. In this simulation, the grid size Δx is about $7\times$ the electron Debye length λ_{De0} based on the background parameters. Though at such a low resolution with kinetic scales severely under-resolved, the simulation remains stable and the time evolution stages of various structures are correctly reproduced.

4.5. Solar wind-magnetosphere interaction at the Earth

Finally, we present results of 3D, large scale simulation of the Earth's magnetosphere under the impact of solar wind plasmas transported from the sun (from the left side of the perspective view in Fig. 5). The system's evolution is largely controlled by magnetic reconnection at both the sun-facing day-side and the trailing night-side. At the dayside, this happens between the Earth's dipolar magnetic field and the southward interplanetary magnetic field. At the nightside, it is between the highly stretched dipolar field. Both reconnection scenarios are clearly captured in the simulation. Later, we will demonstrate the tail reconnection as an example.

The simulation domain has the Earth at the origin, the x-axis is along the Sun-Earth line and points to the Sun, and the z-direction is northward. The domain spans $[-63, 17]$ along x in units of the Earth's radii, and $[-81, 81]$ in the other two directions. A structured stretched nonuniform grid of total size $1600 \times 2200 \times 2200$ is used to achieve high resolution, up to $\Delta x \approx 0.15 R_{\text{Earth}} \approx 2d_e$, near the Earth and near the day- and night-side reconnection sites. Here, d_e is the electron inertia

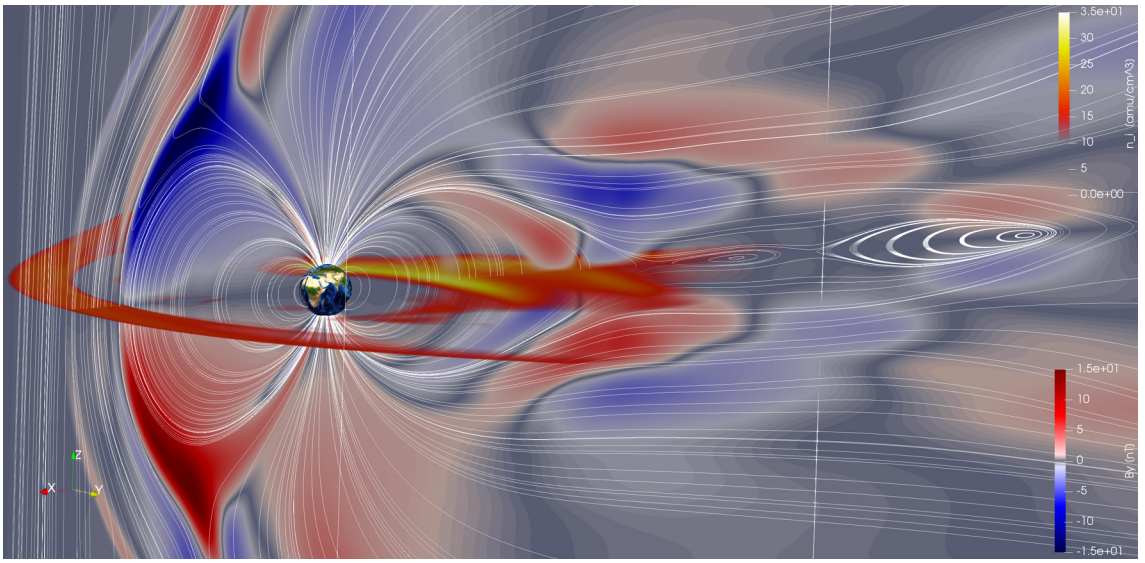

Fig. 5. Perspective view of the Earth's magnetosphere from a Ten-Moment simulation. The solar wind impinges from the left side and carries southward interplanetary magnetic field. The white streamlines are magnetic field lines in the meridional plane (*xz*-plane, which is approximately the paper plane), indicating the thinning of a current sheet on the night-side, along with two plasmoids. The blue-red contours in the *xz*-plane represent the *y* component of the magnetic field due to the Hall term intrinsic to the model. The yellow-scale contours in the *xy*-plane represent ion number density. Its sharp boundary at the dayside (left side) marks the bow shock due to the supersonic and superAlfvénic solar wind flow. (For interpretation of the colors in the figure(s), the reader is referred to the web version of this article.)

length in the solar wind. Further away from Earth and the reconnection regions, the grid resolution ramps down to as low as $\Delta x \approx 20 R_{\text{Earth}}$. During the simulation, the following fixed solar wind density, velocity, pressure, and magnetic field are applied at the upstream boundary at $x = 17 R_{\text{Earth}}$:

$$\rho_{\text{sw}} = 5\,\text{amu/cm}^3,\ \mathbf{v}_{\text{sw}} = [-400,\ 0,\ 0]\ \text{km/s},\ p_{\text{sw}} = 3.45 \times 10^{-12}\,\text{Pa};\ \mathbf{B} = [0,\ 0,\ -5]\ \text{nT}.$$

All other outer boundaries are open and perturbations are allowed to exit the domain. Other simulation parameters include

$$\frac{m_i}{m_e} = 25,\ \frac{p_{e,\text{sw}}}{p_{i,\text{sw}}} = 8,\ \frac{d_{i,\text{sw}}}{R_{\text{Earth}}} = 0.375,\ c = 3000\,\text{km/s}.$$

Here, m_s, $p_{s,\text{sw}}$, and $d_{s,\text{sw}}$ are the mass, pressure, and inertial length of the species s (electron or proton ion), and c is the speed of light artificially reduced to lower the computational cost. The simulation lasted $3600s$ in physical time, and took about 2 million core hours to finish on Pleiades, a petascale supercomputer housed at the NASA Advanced Supercomputing (NAS) facility.

Figure (5) shows a perspective view snapshot. The yellow-white-coded contours represent the ion number density in the equatorial plane. Their dayside boundaries mark the sharp shock due to the supersonic and superAlfvénic inflow. The blue-red-coded contours are the non-vanishing B_y in the xz plane due to the Hall effect contained in the multifluid model. The white streamlines are magnetic field lines in the same plane. The snapshot clearly shows the formation of plasmoids, an coherent structure containing isolated regions of magnetic fluxes. The relaxation of field lines after ejection and the birth of a new plasmoid are depicted in the last two frames, indicating a repeating life-cycle of the system.

Solar wind-magnetosphere interaction is a critical link of the space weather cascade chain. The locally implicit source algorithm discussed here allows efficient multifluid-Maxwell simulations of such global systems by stepping over small kinetic scales that are not important in most of the simulation domain. In general, planetary/moon magnetosphere physics are complicated system sciences. Interested readers may refer to [32,33] for applications of this model to other magnetosphere systems.

5. Conclusions

Multifluid-Maxwell models have been rapidly gaining interest recently in laboratory, space, and astrophysical plasma physics modeling [4,34,33,23,35,22,36,37,11,38–43]. In this paper, we have developed a locally implicit schemes to integrate the source terms for such systems. Numerical restrictions due to kinetic scales like plasma and cyclotron frequencies are eliminated. The calculation involves only local (one-cell) inversion of a $3S + 3$ matrix, where S is the number of species. Direct formulae that avoid null calculations in full matrix operations are derived that can be used to speed up the algorithm. The stability of the source term solver alone and the complete coupled system is validated using a few benchmark problems,

ranging from small, idealized problems to large, complex systems. For completeness, we also derived the exact solutions to the source term equations, which is often more expensive to compute but nevertheless can be implemented as a base benchmark solver.

Eliminating the restrictions due to kinetic scales is crucial for the practical application of the multifluid-Maxwell model. The coupled system is still constrained by the CFL condition due to speed of light, but this is often a less demanding requirement. The locally implicit algorithm enables us to model large, multi-scale systems by stepping over smallest scale physics that might not be crucial for the global picture. In fact, we have successfully applied our model to plasmas in a vast range of problems [4,32,34,33,27,5,46,44,45]. The capability to retain finite order kinetic physics (Hall term, electron inertia, pressure non-gyrotropy etc.) of the coupled multifluid-Maxwell model is desirable for the study of many problems, e.g., magnetic reconnection and turbulence. It is of course also convenient to be able to incorporate an arbitrary number of plasma species, particularly electron physics and multi-ion effects.

One notable difference between our model and the Hall MHD model is that, in the former, the time step size does not go infinitesimal as the dispersive whistler modes grow. In the multifluid-Maxwell model, the whistler wave frequency is correctly limited by the finite electron cyclotron frequency instead of growing to infinity at small wavelengths like in the case of Hall MHD [8,4]. This limitation of Hall MHD could be eliminated by employing sophisticated fully implicit algorithms, the development of which, however, remains a very challenging research topic [47,48].

Several improvements remain open for future work. Particularly, our algorithm is not asymptotic-preserving (AP), i.e., our discretized multifluid-Maxwell equations do not approach the discretized MHD equations as the grid size increases. It is possible to follow existing AP Particle-in-Cell methods (e.g., [49]) to devise an AP multifluid-Maxwell algorithm, with the help of theoretical framework given in Ref. [9]. Another frontier is the search for improved closures to capture nonlocal, kinetic physics that are critical in many applications [5,11,10,12].

Declaration of competing interest

The authors declare that they have no known competing financial interests or personal relationships that could have appeared to influence the work reported in this paper.

Acknowledgements

The authors thank Dr. Peifeng Fan for useful discussions. This work was supported by Air Force Office of Scientific Research under Grant No. FA9550-15-1-0193, DOE grant No. DEAC02-09CH11466, NSF Grant Nos. AGS0962698 and AGS-1338944, NASA Grants Nos. NNH13AW51I, 80NSSC19K0621, 80NSSC18K0288, 80NSSC20K0147 and NNX13AK31G. Resources supporting this work were provided by the NASA High-End Computing (HEC) Program through the NASA Advanced Supercomputing (NAS) Division at Ames Research Center, the National Energy Research Scientific Computing Center, a DOE Office of Science User Facility supported by the Office of Science of the U.S. Department of Energy under Contract No. DE-AC02-05CH11231, Cheyenne (https://doi.org/10.5065/D6RX99HX) provided by NCAR's CISL, sponsored by NSF, and Trillian, a Cray XE6m-200 supercomputer at the UNH supported by the NSF MRI program under Grant No. PHY-1229408.

Appendix A. Useful notes on the matrix form of the linear system of equations

A.1. Notes on skew-symmetric and skew-Hermitian matrices

A square matrix $\mathbf{M}$ is skew-Hermitian if and only if its conjugate transpose is its negative,

$$M_{ij}^{*} = -M_{ji}. \tag{A.1}$$

Here the superscript * represents the conjugate operation.

The following properties of a skew-Hermitian matrix $\mathbf{M}$ are useful in our derivation:

- $\mathbf{M}$ is diagonalizable and all of its eigenvalues are either purely imaginary or zero.
- Eigenvectors of distinct eigenvalues of $\mathbf{M}$ are orthogonal to each other.
- If $\mathbf{M}$ is also real, then its nonzero eigenvalues come in pairs $\pm\lambda$.
  - Now if $\mathbf{v}$ is an eigenvector of $\mathbf{M}$ with eigenvalue $\lambda = i\omega$ then $\mathbf{v}^{*}$ is an eigenvector for eigenvalue $-i\omega$.
- $i\mathbf{M}$ is Hermitian.
- If $\mathbf{v}$ is an eigenvector of $\mathbf{M}$ with eigenvalue $\lambda = i\omega$, it is an eigenvalue of $i\mathbf{M}$ with eigenvalue ω.

A.2. Equivalent eigenvalue problem

Note that solving the constant-coefficient linear ODE system

$$\frac{\partial \mathbf{q}}{\partial t} = \mathbf{M} \cdot \mathbf{q}, \tag{A.2}$$

where $\mathbf{M}$ is a skew-Hermitian matrix, is equivalent to solving the time-independent eigenvalue problem

$$\mathbf{M} \cdot \mathbf{v}_\ell = \mathbf{v}_\ell \lambda_\ell \tag{A.3}$$

Here λ_ℓ and $\mathbf{v}_\ell$ are the ℓth eigenvalue and eigenvector of $\mathbf{M}$.

To solve the initial value problem, we need to first compute the eigencoefficients c_ℓ by projecting the initial condition onto the eigenvectors,

$$\mathbf{q}(t=0) = \sum_\ell c_\ell \mathbf{v}_\ell . \tag{A.4}$$

The temporal evolution then follows

$$\mathbf{q}(t) = \sum_\ell c_\ell \mathbf{v}_\ell \exp(\lambda_\ell t) . \tag{A.5}$$

Since $\mathbf{M}$ is skew-Hermitian, λ_ℓ must be purely imaginary or zero. Therefore the solution above is oscillatory or constant in time.

In addition, due to the theory of skew-Hermitian matrices, their eigenvectors for distinct eigenvalues must be orthogonal. Therefore we can compute the coefficients for nondegenerate eigenvectors by

$$c_\ell = \mathbf{q}(t=0) \cdot \mathbf{v}_\ell . \tag{A.6}$$

Note that the degenerate eigenvectors might not be orthogonal, though.

A.3. Constructing real solutions

The solution Eqn. (A.5) can be complex. Thus we need to construct real solutions from them to represent real physical values. To do this, we first consider a complex eigenvector $\mathbf{v} = \mathbf{a} + i\,\mathbf{b}$ of an eigenvalue $\lambda = i\omega$, the corresponding time-dependent, complex solution to Eqn. (A.2) is

$$\begin{aligned} \mathbf{v}\exp(i\omega t) &= (\mathbf{a} + i\mathbf{b})(\cos\omega t + i\sin\omega t) \\ &= \mathbf{a}\cos\omega t - \mathbf{b}\sin\omega t + i(\mathbf{a}\sin\omega t + \mathbf{b}\cos\omega t) . \end{aligned} \tag{A.7}$$

Note that $-i\mathbf{v}$ is also an eigenvector with eigenvalue $i\omega$ and has the time-dependent solution

$$\begin{aligned} \mathbf{v}\exp(i\omega t) &= (\mathbf{b} - i\mathbf{a})(\cos\omega t + i\sin\omega t) \\ &= \mathbf{a}\sin\omega t + \mathbf{b}\cos\omega t - i(\mathbf{a}\cos\omega t - \mathbf{b}\sin\omega t) . \end{aligned} \tag{A.8}$$

Thus we identify two independent real solution bases

$$\mathbf{a}\cos\omega t - \mathbf{b}\sin\omega t \text{ and } \mathbf{a}\sin\omega t + \mathbf{b}\cos\omega t \tag{A.9}$$

which are the real and imaginary parts of Eqn. (A.7). In other words, to construct the real solutions, we only need to take the real and imaginary parts of an complex eigenvector Eqn. (A.7).

Appendix B. Deriving the exact solutions

For a single grid cell, the procedure to update the source term Eqn. (18) by a time step Δt can be outlined below:

Algorithm 1 Update source term Eqn. (18) exactly in one cell.

```
Normalize E and J_s to get anti-symmetric; coefficient matrix for Eqn. (18)
if If |B| ≠ 0 then
    Decompose the system into a parallel part and a perpendicular part regarding B;
    for sub-system in {parallel, perpendicular} do
        Compute eigenvalues and eigenvectors of the coefficient matrix at t = 0;
        Compute eigencoefficients by projecting the initial state onto the eigenvectors;
        Compute eigenvectors at t = Δt;
        Compute the updated state at t = Δt as combinations of the updated eigenvectors;
else
    Solve the equivalent parallel problem along all three directions;
Normalize E and J_s back to their original units;
```

B.1. Normalization towards an anti-symmetric system

This section addresses the line 1 in Algorithm 1. Eqn. (18) for N species can be written in a matrix form

$$\frac{\partial}{\partial t}\begin{bmatrix}\mathbf{E}\\ \mathbf{J}_1\\ \mathbf{J}_2\\ \vdots\\ \mathbf{J}_N\end{bmatrix}=\begin{bmatrix}0 & -1/\varepsilon_0 & -1/\varepsilon_0 & \cdots & -1/\varepsilon_0\\ \omega_1^2\varepsilon_0 & -\boldsymbol{\Omega}_1\times\mathcal{I} & 0 & \cdots & 0\\ \omega_2^2\varepsilon_0 & 0 & -\boldsymbol{\Omega}_2\times\mathcal{I} & \cdots & 0\\ \vdots & \vdots & \vdots & \ddots & \vdots\\ \omega_N^2\varepsilon_0 & 0 & 0 & \cdots & -\boldsymbol{\Omega}_N\times\mathcal{I}\end{bmatrix}\begin{bmatrix}\mathbf{E}\\ \mathbf{J}_1\\ \mathbf{J}_2\\ \vdots\\ \mathbf{J}_{N-1}\\ \mathbf{J}_N\end{bmatrix}, \tag{B.1}$$

where $\mathcal{I}$ is a 3×3 unit tensor, ω_s and $\boldsymbol{\Omega}_s$ denote the plasma and signed cyclotron frequency of species s

$$\omega_s\equiv\sqrt{\frac{q_s^2 n_s}{\varepsilon_0 m_s}},\quad \boldsymbol{\Omega}_s\equiv\frac{q_s\mathbf{B}}{m_s}. \tag{B.2}$$

It is easier to work with a symmetric or antisymmetric system. This can be achieved by renormalizing the electric field and currents. Normalizing E_0 and J_{s0} so that

$$\mathbf{E}=\tilde{\mathbf{E}}E_0,\quad \mathbf{J}_s=\tilde{\mathbf{J}}_s J_{s0}, \tag{B.3}$$

and require

$$J_{s0}/\varepsilon_0 E_0=\omega_{ps}, \tag{B.4}$$

the system becomes anti-symmetric:

$$\frac{\partial}{\partial t}\begin{bmatrix}\tilde{\mathbf{E}}\\ \tilde{\mathbf{J}}_1\\ \tilde{\mathbf{J}}_2\\ \vdots\\ \tilde{\mathbf{J}}_N\end{bmatrix}=\begin{bmatrix}0 & -\omega_1 & -\omega_2 & \cdots & -\omega_N\\ \omega_1 & -\boldsymbol{\Omega}_1\times\mathcal{I} & 0 & \cdots & 0\\ \omega_2 & 0 & -\boldsymbol{\Omega}_2\times\mathcal{I} & \cdots & 0\\ \vdots & \vdots & \vdots & \ddots & \vdots\\ \omega_N & 0 & 0 & \cdots & -\boldsymbol{\Omega}_N\times\mathcal{I}\end{bmatrix}\begin{bmatrix}\tilde{\mathbf{E}}\\ \tilde{\mathbf{J}}_1\\ \tilde{\mathbf{J}}_2\\ \vdots\\ \tilde{\mathbf{J}}_N\end{bmatrix}. \tag{B.5}$$

Eqn. (B.5) can be further decomposed into a parallel part and a perpendicular part with regard to the background magnetic field direction. We shall solve these two parts separately.

B.2. Parallel sub-system

This section identifies the eigenvectors needed in the loop 4 of Algorithm 1 for the *parallel* sub-system. This sub-system evolves $(\mathbf{E}_\parallel;\mathbf{u}_{s\parallel})$ and writes

$$\frac{\partial}{\partial t}\begin{bmatrix}\tilde{\mathbf{E}}_\parallel\\ \tilde{\mathbf{J}}_{1\parallel}\\ \tilde{\mathbf{J}}_{2\parallel}\\ \vdots\\ \tilde{\mathbf{J}}_{N\parallel}\end{bmatrix}=\mathbf{M}_\parallel\begin{bmatrix}\tilde{\mathbf{E}}_\parallel\\ \tilde{\mathbf{J}}_{1\parallel}\\ \tilde{\mathbf{J}}_{2\parallel}\\ \vdots\\ \tilde{\mathbf{J}}_{N\parallel}\end{bmatrix}, \tag{B.6}$$

with the coefficient matrix

$$\mathbf{M}_\parallel=\begin{bmatrix}0 & -\omega_1 & -\omega_2 & \cdots & -\omega_N\\ \omega_1 & 0 & 0 & \cdots & 0\\ \omega_2 & 0 & 0 & \cdots & 0\\ \vdots & \vdots & \vdots & \ddots & \vdots\\ \omega_N & 0 & 0 & \cdots & 0\end{bmatrix}. \tag{B.7}$$

$\mathbf{M}_\parallel$ has three distinct eigenvalues $-i\,\omega_p$, $i\,\omega_p$, 0 with multiplicities 1, 1, and $N-1$, respectively. Here, the total plasma frequency ω_p is defined as

$$\omega_p^2\equiv\sum_s\omega_s^2.$$

Following the procedure in Sec. A.2 and A.3, the $N+1$ real solution basis is

$$\begin{bmatrix} \tilde{\mathbf{E}}_{\parallel} \\ \tilde{\mathbf{J}}_{1\parallel} \\ \tilde{\mathbf{J}}_{2\parallel} \\ \vdots \\ \tilde{\mathbf{J}}_{N-1,\parallel} \tilde{\mathbf{J}}_{N\parallel} \end{bmatrix} = \begin{bmatrix} \omega_p \cos(\omega_p t) \\ \omega_1 \sin(\omega_p t) \\ \omega_2 \sin(\omega_p t) \\ \vdots \\ \omega_{N-1} \sin(\omega_p t) \\ \omega_N \sin(\omega_p t) \end{bmatrix}; \begin{bmatrix} -\omega_p \sin(\omega_p t) \\ \omega_1 \cos(\omega_p t) \\ \omega_2 \cos(\omega_p t) \\ \vdots \\ \omega_{N-1} \cos(\omega_p t) \\ \omega_N \cos(\omega_p t) \end{bmatrix}; \begin{bmatrix} 0 \\ 1/\omega_1 \\ 0 \\ \vdots \\ 0 \\ -1/\omega_N \end{bmatrix}, \begin{bmatrix} 0 \\ 0 \\ 1/\omega_2 \\ \vdots \\ 0 \\ -1/\omega_N \end{bmatrix}, \ldots, \begin{bmatrix} 0 \\ 0 \\ 0 \\ \vdots \\ 1/\omega_{N-1} \\ -1/\omega_N \end{bmatrix}. \tag{B.8}$$

At $t=0$, they are

$$\begin{bmatrix} \omega_p \\ 0 \\ 0 \\ \vdots \\ 0 \\ 0 \end{bmatrix}, \begin{bmatrix} 0 \\ \omega_1 \\ \omega_2 \\ \vdots \\ \omega_{N-1} \\ \omega_N \end{bmatrix}, \begin{bmatrix} 0 \\ 1/\omega_1 \\ 0 \\ \vdots \\ 0 \\ -1/\omega_N \end{bmatrix}, \begin{bmatrix} 0 \\ 0 \\ 1/\omega_2 \\ \vdots \\ 0 \\ -1/\omega_N \end{bmatrix}, \ldots, \begin{bmatrix} 0 \\ 0 \\ 0 \\ \vdots \\ 1/\omega_{N-1} \\ -1/\omega_N \end{bmatrix}. \tag{B.9}$$

Note that the $N-1$ degenerate eigenvectors for $\omega_{\parallel}=0$ are not orthogonal when $N \geq 3$. Thus we cannot compute their eigencoefficients following Eqn. (A.6) directly. Instead, we would have to orthogonalize these eigenvectors (using, e.g., the Gram-Schmidt procedure) first. However, we note that these eigenvectors do not change in time. As a result, we do not need to project onto them. The solution at t can be computed by simply accumulating the incremental changes due to the first two basis vectors only. In other words, we only need to do projection onto the first and the second basis vectors in Eqn. (B.9), i.e., to compute c_0 and c_1 following Eqn. (A.6). The updated state at time $t=\Delta t$ is

$$\mathbf{q}_{\parallel}(t=\Delta t) = \mathbf{q}_{\parallel}(t=0) + c_0 \begin{bmatrix} \omega_p \left[\cos(\omega_p \Delta t) - 1\right] \\ \omega_1 \sin(\omega_p \Delta t) \\ \omega_2 \sin(\omega_p \Delta t) \\ \vdots \\ \omega_{N-1} \sin(\omega_p \Delta t) \\ \omega_N \sin(\omega_p \Delta t) \end{bmatrix} + c_1 \begin{bmatrix} -\omega_p \sin(\omega_p \Delta t) \\ \omega_1 \left[\cos(\omega_p \Delta t) - 1\right] \\ \omega_2 \left[\cos(\omega_p \Delta t) - 1\right] \\ \vdots \\ \omega_{N-1} \left[\cos(\omega_p \Delta t) - 1\right] \\ \omega_N \left[\cos(\omega_p \Delta t) - 1\right] \end{bmatrix}. \tag{B.10}$$

B.3. Perpendicular sub-system

This section identifies the eigenvectors needed in the loop 4 of Algorithm 1 for the *perpendicular* sub-system. To get an elegant form of the sub-system, consider the two perpendicular components of a vector as the real and imaginary parts of a complex vector, i.e., $\tilde{\mathbf{E}}_{\perp} = \tilde{E}_1 + i\tilde{E}_2$, etc. Then we can write the perpendicular system as

$$\frac{\partial}{\partial t} \begin{bmatrix} \tilde{\mathbf{E}}_{\perp} \\ \tilde{\mathbf{J}}_{1\perp} \\ \tilde{\mathbf{J}}_{2\perp} \\ \vdots \\ \tilde{\mathbf{J}}_{N-1,\perp} \\ \tilde{\mathbf{J}}_{N\perp} \end{bmatrix} = \mathbf{M}_{\perp} \cdot \begin{bmatrix} \tilde{\mathbf{E}}_{\perp} \\ \tilde{\mathbf{J}}_{1\perp} \\ \tilde{\mathbf{J}}_{2\perp} \\ \vdots \\ \tilde{\mathbf{J}}_{N-1,\perp} \\ \tilde{\mathbf{J}}_{N\perp} \end{bmatrix}, \tag{B.11}$$

where the complex coefficient matrix is

$$\mathbf{M}_{\perp} = \begin{bmatrix} 0 & -\omega_1 & -\omega_2 & \cdots & -\omega_N \\ \omega_1 & -i\,\Omega_1 & 0 & 0 & 0 \\ \omega_2 & 0 & -i\,\Omega_2 & 0 & 0 \\ \vdots & 0 & 0 & \ddots & 0 \\ \omega_N & 0 & 0 & 0 & -i\,\Omega_N \end{bmatrix}. \tag{B.12}$$

Since $\mathbf{M}_{\perp}$ is skew-Hermitian, it has $N+1$ purely imaginary eigenvalues $\lambda_j = i\omega_j$ that can be obtained (see Sec. C) by solving

$$\omega - \sum_s \frac{\omega_s^2}{\omega + \Omega_s} = 0. \tag{B.13}$$

Each eigenvalue has two real, orthogonal solution bases of different polarizations (see Sec. C):

$$\begin{bmatrix} \tilde{E}_1 \\ \tilde{E}_2 \\ \vdots \\ \tilde{J}_{s1} \\ \tilde{J}_{s2} \\ \vdots \end{bmatrix} = \begin{bmatrix} -\sin\omega t \\ \cos\omega t \\ \vdots \\ \frac{\omega_s}{\omega+\Omega_s}\cos\omega t \\ \frac{\omega_s}{\omega+\Omega_s}\sin\omega t \\ \vdots \end{bmatrix} \text{ and } \begin{bmatrix} \cos\omega t \\ \sin\omega t \\ \vdots \\ \frac{\omega_s}{\omega+\Omega_s}\sin\omega t \\ -\frac{\omega_s}{\omega+\Omega_s}\cos\omega t \\ \vdots \end{bmatrix}. \tag{B.14}$$

At $t = 0$ they are

$$\begin{bmatrix} E_1 \\ E_2 \\ \vdots \\ u_{1s} \\ u_{2s} \\ \vdots \end{bmatrix} = \begin{bmatrix} 0 \\ 1 \\ \vdots \\ \frac{\omega_s}{\omega+\Omega_s} \\ 0 \\ \vdots \end{bmatrix} \text{ and } \begin{bmatrix} 1 \\ 0 \\ \vdots \\ 0 \\ -\frac{\omega_s}{\omega+\Omega_s} \\ \vdots \end{bmatrix}. \tag{B.15}$$

By the theory of Hermitian matrices, the eigenvectors of distinct eigenvalues are orthogonal. Therefore we recover $2 \times (N+1)$ orthogonal solution basis vectors.

Finally, the time-dependent solution to the original perpendicular sub-system Eqn. (B.11) can be obtained following the "project-and-evolve" procedure outlined in Sec. A.2.

B.4. Exact solution to the pressure tensor rotation

The source term for the pressure tensor rotation, Eqn. (20), can be written more explicitly as

$$\frac{d}{dt}\begin{bmatrix} P_{xx} \\ P_{xy} \\ P_{xz} \\ P_{yy} \\ P_{yz} \\ P_{zz} \end{bmatrix} = \frac{q}{m}\begin{bmatrix} 0 & 2B_y & -2B_y & 0 & 0 & 0 \\ -B_z & 0 & B_x & B_z & -B_y & 0 \\ B_y & -B_x & 0 & 0 & B_z & -B_y \\ 0 & -2B_z & 0 & 0 & 2B_x & 0 \\ 0 & B_y & -B_z & -B_x & 0 & B_x \\ 0 & 0 & 2B_y & 0 & -2B_x & 0 \end{bmatrix}\begin{bmatrix} P_{xx} \\ P_{xy} \\ P_{xz} \\ P_{yy} \\ P_{yz} \\ P_{zz} \end{bmatrix}. \tag{B.16}$$

It can be solved analytically, too, and can be implemented following Algorithm 2. The rotation matrix $\mathbf{R}$ in line 2 of

Algorithm 2 Update source term for pressure tensor equation for species s exactly in one cell.

1: Compute the rotation angle $\alpha(\Delta t) = -\Omega_{cs}\Delta t$ counter-clockwise around $\mathbf{B}$;
2: Compute the rotation matrix $\mathbf{R}$ for α;
3: Rotate the pressure tensor $\mathbf{P}$ by applying the rotation matrix $\mathbf{R}$;

Algorithm 2 is

$$\mathbf{R} = \begin{bmatrix} \cos\alpha + (1-\cos\alpha)b_1^2, & (1-\cos\alpha)b_1b_2 - \sin\alpha\, b_3, & (1-\cos\alpha)b_1p_3 + \sin\alpha\, b_2 \\ (1-\cos\alpha)b_2b_1 + \sin\alpha\, b_3, & \cos\alpha + (1-\cos\alpha)b_2^2, & (1-\cos\alpha)b_2p_3 - \sin\alpha\, b_1 \\ (1-\cos\alpha)b_3b_1 - \sin\alpha\, b_2, & (1-\cos\alpha)b_3b_2 + \sin\alpha\, b_1, & \cos\alpha + (1-\cos\alpha)b_3^2 \end{bmatrix}. \tag{B.17}$$

The pressure tensor rotation in line 3 can be performed as

$$\mathbf{P}(\Delta t) = \mathbf{R}\cdot\mathbf{P}(0)\cdot\mathbf{R}^T, \tag{B.18}$$

in the expanded form

$$\begin{aligned} P_{mn}(t) &= \sum_i\sum_j P_{ij}(0)\, R_{mi}R_{nj} \\ &= P_{11}(0)\, R_{m1}R_{n1} + P_{21}(0)\, R_{m2}R_{n1} + P_{31}(0)\, R_{m3}R_{n1} \\ &+ P_{12}(0)\, R_{m1}R_{n3} + P_{22}(0)\, R_{m2}R_{n2} + P_{32}(0)\, R_{m3}R_{n2} \\ &+ P_{13}(0)\, R_{m1}R_{n3} + P_{23}(0)\, R_{m2}R_{n3} + P_{33}(0)\, R_{m3}R_{n3}. \end{aligned} \tag{B.19}$$

Appendix C. More details on the exact solution of the perpendicular sub-system

The perpendicular system evolves $(\mathbf{E}_\perp; \mathbf{u}_{s\perp})$ and writes

$$\frac{\partial}{\partial t}\begin{bmatrix} \tilde{\mathbf{E}}_{\perp 1} \\ \tilde{\mathbf{E}}_{\perp 2} \\ \tilde{\mathbf{J}}_{1\perp 1} \\ \tilde{\mathbf{J}}_{1\perp 2} \\ \tilde{\mathbf{J}}_{2\perp 1} \\ \tilde{\mathbf{J}}_{2\perp 2} \\ \vdots \\ \tilde{\mathbf{J}}_{N\perp 1} \\ \tilde{\mathbf{J}}_{N\perp 2} \end{bmatrix} = \begin{bmatrix} 0 & 0 & -\omega_1 & 0 & -\omega_1 & 0 & \cdots & -\omega_N & 0 \\ 0 & 0 & 0 & -\omega_1 & 0 & -\omega_1 & \cdots & 0 & -\omega_N \\ \omega_1 & 0 & 0 & \Omega_1 & 0 & 0 & \cdots & 0 & 0 \\ 0 & \omega_1 & -\Omega_1 & 0 & 0 & 0 & \cdots & 0 & 0 \\ \omega_2 & 0 & 0 & 0 & 0 & \Omega_2 & \cdots & 0 & 0 \\ 0 & \omega_2 & 0 & 0 & -\Omega_2 & 0 & \cdots & 0 & 0 \\ \vdots & \vdots & \vdots & \vdots & \vdots & \vdots & \ddots & \vdots & \vdots \\ \omega_N & 0 & 0 & 0 & 0 & 0 & \cdots & 0 & \Omega_N \\ 0 & \omega_N & 0 & 0 & 0 & 0 & \cdots & -\Omega_N & 0 \end{bmatrix} \cdot \begin{bmatrix} \tilde{\mathbf{E}}_{\perp 1} \\ \tilde{\mathbf{E}}_{\perp 2} \\ \tilde{\mathbf{J}}_{1\perp 1} \\ \tilde{\mathbf{J}}_{1\perp 2} \\ \tilde{\mathbf{J}}_{2\perp 1} \\ \tilde{\mathbf{J}}_{2\perp 2} \\ \vdots \\ \tilde{\mathbf{J}}_{N\perp 1} \\ \tilde{\mathbf{J}}_{N\perp 2} \end{bmatrix}. \tag{C.1}$$

Here the subscripts $_1$ and $_2$ represent two orthogonal directions that form a right-handed coordinate when combined with the background magnetic field direction (along direction "3").

Note that the coefficient matrix of Eq. (C.1) is a $2(N+1)\times 2(N+1)$ real, skew-symmetric matrix. Its nonzero eigenvalues are purely imaginary and come in pairs $\pm i\omega$ with conjugate eigenvectors. In total, the system has $2(N+1)$ eigenvalues and eigenvectors. However, to simplify the problem, we may consider the two components of a perpendicular vector as the real and imaginary parts of a complex vector, the equation above can be rearranged into a more compact form Eq. (B.11). The coefficient matrix $\mathbf{M}_\perp$ now is a $(N+1)\times(N+1)$ skew-Hermitian matrix and has $N+1$ complex eigenvectors. The real and imaginary parts of the eigenvectors serve as the 1st and 2nd components of the perpendicular vectors, as we will see below.

C.1. Eigenvalues

Consider the eigenstructure of the perpendicular problem Eq. (B.11),

$$0 = \left(\mathbf{M}_\perp - i\omega\hat{\mathbf{I}}\right)\cdot\mathbf{q}_\perp = \begin{bmatrix} -i\omega & -\omega_1 & -\omega_2 & \cdots & -\omega_N \\ \omega_1 & -i(\omega+\Omega_1) & 0 & 0 & 0 \\ \omega_2 & 0 & -i(\omega+\Omega_2) & 0 & 0 \\ \vdots & 0 & 0 & \ddots & 0 \\ \omega_N & 0 & 0 & 0 & -i(\omega+\Omega_N) \end{bmatrix}\cdot\mathbf{q}_\perp. \tag{C.2}$$

The first row gives

$$-i\omega\tilde{\mathbf{E}}_\perp = \sum_s \omega_s\tilde{\mathbf{J}}_{s\perp} \tag{C.3}$$

while the remaining rows simultaneously give

$$\tilde{\mathbf{E}}_\perp\omega_s - i(\omega+\Omega_s)\tilde{\mathbf{J}}_{\perp s} = 0, \text{ where } s = 1,\ldots,N \tag{C.4}$$

$$\Rightarrow \tilde{\mathbf{J}}_{\perp s} = \tilde{\mathbf{E}}_\perp\frac{\omega_s}{i(\omega+\Omega_s)}. \tag{C.5}$$

Substitute Eq. (C.5) into Eq. (C.3) leads to

$$-i\omega\tilde{\mathbf{E}}_\perp = \sum_s \omega_s\frac{\omega_s}{i(\omega+\Omega_s)}\tilde{\mathbf{E}}_\perp = -i\sum_s\frac{\omega_s^2}{\omega+\Omega_s}\tilde{\mathbf{E}}_\perp \tag{C.6}$$

or

$$\tilde{\mathbf{E}}_\perp\left(\omega - \sum_s\frac{\omega_s^2}{\omega+\Omega_s}\right) = 0 \tag{C.7}$$

which has nontrivial solution of $\tilde{\mathbf{E}}_\perp$ when and only when Eq. (B.13) is satisfied. Since $\mathbf{M}_\perp$ is skew-Hermitian and $i\mathbf{M}_\perp$ is Hermitian, solving the equation above gives $N+1$ real eigenvalues ω for $i\mathbf{M}_\perp$ and correspondingly $N+1$ imaginary eigenvalues $\lambda = i\omega$ for $\mathbf{M}_\perp$.

Eq. (B.13) can be expanded as a $N+1$ order polynomial and solved with any root finder. For three or fewer species, analytic formulae exists for the roots. For more species, we may find the roots as eigenvalues of a companion matrix, or using an iterative root finder.

C.2. Eigenvectors

As indicated by Eq. (C.5), for each eigenvalue $i\omega$, there are two complex eigenvectors

$$\begin{bmatrix} i \\ \frac{\omega_1}{\omega+\Omega_1} \\ \frac{\omega_2}{\omega+\Omega_2} \\ \frac{\omega_3}{\omega+\Omega_3} \\ \frac{\omega_4}{\omega+\Omega_4} \end{bmatrix} \text{ and } \begin{bmatrix} 1 \\ -i\frac{\omega_1}{\omega+\Omega_1} \\ -i\frac{\omega_2}{\omega+\Omega_2} \\ -i\frac{\omega_3}{\omega+\Omega_3} \\ -i\frac{\omega_4}{\omega+\Omega_4} \end{bmatrix}. \tag{C.8}$$

C.3. Real solution bases

From these two complex eigenvectors, we can determine two time-dependent real, orthogonal solution bases following the recipe in Sec. A.3. To determine the first real solution, we first write down the full, complex eigenvector of $\lambda = i\omega$ as

$$\mathbf{v} = \mathbf{a} + i\mathbf{b}, \text{ where } \mathbf{a} = \begin{bmatrix} 0 \\ \frac{\omega_1}{\omega+\Omega_1} \\ \frac{\omega_2}{\omega+\Omega_2} \\ \frac{\omega_3}{\omega+\Omega_3} \\ \frac{\omega_4}{\omega+\Omega_4} \end{bmatrix}, \mathbf{b} = \begin{bmatrix} 1 \\ 0 \\ 0 \\ 0 \\ 0 \end{bmatrix}, \tag{C.9}$$

then the time-dependent solution for the perpendicular problem is

$$\begin{aligned} \mathbf{v}e^{i\omega t} &= (\mathbf{a} + i\mathbf{b})(\cos\omega t + i\sin\omega t) \\ &= (\mathbf{a}\cos\omega t - \mathbf{b}\sin\omega t) + i(\mathbf{a}\sin\omega t + \mathbf{b}\cos\omega t) \\ &= \begin{bmatrix} -\sin\omega t \\ \frac{\omega_1}{\omega+\Omega_1}\cos\omega t \\ \frac{\omega_2}{\omega+\Omega_2}\cos\omega t \\ \frac{\omega_3}{\omega+\Omega_3}\cos\omega t \\ \frac{\omega_4}{\omega+\Omega_4}\cos\omega t \end{bmatrix} + i \begin{bmatrix} \cos\omega t \\ \frac{\omega_1}{\omega+\Omega_1}\sin\omega t \\ \frac{\omega_2}{\omega+\Omega_2}\sin\omega t \\ \frac{\omega_3}{\omega+\Omega_3}\sin\omega t \\ \frac{\omega_4}{\omega+\Omega_4}\sin\omega t \end{bmatrix}. \end{aligned} \tag{C.10}$$

The real and imaginary parts in each row are the first and second components of a same perpendicular vector $\tilde{\mathbf{E}}_\perp$ or $\tilde{\mathbf{J}}_{s\perp}$. Thus the time-dependent real solution is

$$\begin{bmatrix} \tilde{E}_1 \\ \tilde{E}_2 \\ \vdots \\ J_{s1} \\ \tilde{J}_{s2} \\ \vdots \end{bmatrix} = \begin{bmatrix} -\sin\omega t \\ \cos\omega t \\ \vdots \\ \frac{\omega_s}{\omega+\Omega_s}\cos\omega t \\ \frac{\omega_s}{\omega+\Omega_s}\sin\omega t \\ \vdots \end{bmatrix}. \tag{C.11}$$

Similarly, the second time-dependent real solution can be determined by

$$\mathbf{v} = \mathbf{a} + i\mathbf{b}, \text{ where } \mathbf{a} = \begin{bmatrix} 1 \\ 0 \\ 0 \\ 0 \\ 0 \end{bmatrix}, \mathbf{b} = -\begin{bmatrix} 0 \\ \frac{\omega_1}{\omega+\Omega_1} \\ \frac{\omega_2}{\omega+\Omega_2} \\ \frac{\omega_3}{\omega+\Omega_3} \\ \frac{\omega_4}{\omega+\Omega_4} \end{bmatrix}, \tag{C.12}$$

$$\begin{aligned} \Rightarrow \mathbf{v}e^{i\omega t} &= (\mathbf{a} + i\mathbf{b})(\cos\omega t + i\sin\omega t) \\ &= (\mathbf{a}\cos\omega t - \mathbf{b}\sin\omega t) + i(\mathbf{a}\sin\omega t + \mathbf{b}\cos\omega t) \\ &= \begin{bmatrix} \cos\omega t \\ \frac{\omega_1}{\omega+\Omega_1}\sin\omega t \\ \frac{\omega_2}{\omega+\Omega_2}\sin\omega t \\ \frac{\omega_3}{\omega+\Omega_3}\sin\omega t \\ \frac{\omega_4}{\omega+\Omega_4}\sin\omega t \end{bmatrix} + i \begin{bmatrix} \sin\omega t \\ -\frac{\omega_1}{\omega+\Omega_1}\cos\omega t \\ -\frac{\omega_2}{\omega+\Omega_2}\cos\omega t \\ -\frac{\omega_3}{\omega+\Omega_3}\cos\omega t \\ -\frac{\omega_4}{\omega+\Omega_4}\cos\omega t \end{bmatrix}. \end{aligned} \tag{C.13}$$

The second real solution is then

$$\begin{bmatrix} \tilde{E}_1 \\ \tilde{E}_2 \\ \vdots \\ J_{s1} \\ \tilde{J}_{s2} \\ \vdots \end{bmatrix} = \begin{bmatrix} \cos\omega t \\ \sin\omega t \\ \vdots \\ \frac{\omega_s}{\omega+\Omega_s}\sin\omega t \\ -\frac{\omega_s}{\omega+\Omega_s}\cos\omega t \\ \vdots \end{bmatrix}. \tag{C.14}$$

Now we find two real, orthogonal solutions for $\lambda = i\omega$ of different polarizations as in Eq. (B.14). In total, we recover all $2\times(N+1)$ real, orthogonal solutions to the $2(N+1)$ order Eq. (C.1).

Appendix D. Direct calculation of the locally implicit scheme

The linear, constant-coefficient ODEs Eqns. (30) can be solved directly instead of through matrix inversion, as described in Ref. [25]. This usually leads to faster computation. Here, we give a straightforward derivation, and fix a few minor mistakes in Ref. [25]. Note that we do not consider collisions, while Ref. [25] did.

We start by noting that the general problem

$$\mathbf{A} = \mathbf{R} + \mathbf{A}\times\mathbf{B}, \tag{D.1}$$

where $\mathbf{R}$ and $\mathbf{B}$ are knowns, has the solution

$$\mathbf{A} = \frac{\mathbf{R} + \mathbf{B}\mathbf{B}\cdot\mathbf{R} - \mathbf{B}\times\mathbf{R}}{1+B^2} = \frac{\mathbf{R} + B^2\mathbf{b}\mathbf{b}\cdot\mathbf{R} - B\mathbf{b}\times\mathbf{R}}{1+B^2}. \tag{D.2}$$

A relevant problem

$$\mathbf{C} = \mathbf{R} + \mathbf{C}\times\mathbf{B} + \xi\mathbf{b}\mathbf{b}\cdot\mathbf{C}, \tag{D.3}$$

where $\xi \neq 1$ and $\mathbf{b}$ is the unit vector along $\mathbf{B}$, has the solution

$$\mathbf{C} = \frac{\mathbf{R} + \mathbf{B}\mathbf{B}\cdot\mathbf{R} - \mathbf{B}\times\mathbf{R}}{1+B^2} + \frac{\xi}{1-\xi}\mathbf{b}\mathbf{b}\cdot\mathbf{R}. \tag{D.4}$$

The first line of Eqns. (30) can be re-arranged into the form of Eqn. (D.1),

$$\bar{\mathbf{J}}_s = \left(\mathbf{J}_s^n + \frac{\varepsilon_0\omega_s^2\Delta t}{2}\bar{\mathbf{E}}\right) + \bar{\mathbf{J}}_s\times\left(\frac{\Omega_s\Delta t}{2}\mathbf{b}\right), \tag{D.5}$$

thus has the solution

$$\bar{\mathbf{J}}_s = \left(1+\frac{\Omega_s^2\Delta t^2}{4}\right)^{-1}\left(\mathbf{J}_s^* + \frac{\Omega_s^2\Delta t^2}{4}\mathbf{b}\mathbf{b}\cdot\mathbf{J}_s^* - \mathbf{b}\times\frac{\Omega_s\Delta t}{2}\mathbf{J}_s^*\right), \tag{D.6}$$

where

$$\mathbf{J}_s^* \equiv \mathbf{J}_s^n + \frac{\varepsilon_0\omega_s^2\Delta t}{2}\bar{\mathbf{E}}. \tag{D.7}$$

Note that Eqn. (15) of Ref. [25] corresponds to Eqn. ((D.6)) above, but it misses a leading coefficient $\left(1+\Omega_s^2\Delta t^2/4\right)^{-1}$ and the dimensionality is not correct.

Substituting Eqn. (D.6) back into the second line of Eqns. (30) yields an equation of $\bar{\mathbf{E}}$ in the form of Eqn. (D.3):

$$\begin{aligned}\mathbf{F}^{n+1/2} = {} & \frac{\mathbf{F}^n + \frac{1}{2}\mathbf{K}}{1+\frac{1}{4}\omega_0^2} + \frac{1}{1+\frac{1}{4}\omega_0^2}\frac{\delta}{8}\mathbf{b}\times\mathbf{F}^{n+1/2} \\ & - \frac{1}{1+\frac{1}{4}\omega_0^2}\frac{\gamma^2}{16}\mathbf{b}\mathbf{b}\cdot\mathbf{F}^{n+1/2},\end{aligned} \tag{D.8}$$

where $\mathbf{F} \equiv \varepsilon_0\mathbf{E}$, and

$$\begin{aligned}\mathbf{K} \equiv -\Delta t\sum_s \Bigg[& \left(1+\frac{\Omega_s^2\Delta t^2}{4}\right)^{-1} \\ & \left(\mathbf{J}_s^n + \frac{\Omega_s^2\Delta t^2}{4}\mathbf{b}\mathbf{b}\cdot\mathbf{J}_s^n - \mathbf{b}\times\frac{\Omega_s\Delta t}{2}\mathbf{J}_s^n\right)\Bigg].\end{aligned} \tag{D.9}$$

Following Eqn. (D.4) and after some rather tedious algebraic re-arrangement, we obtain

$$\begin{aligned}\bar{\mathbf{F}} = &+\frac{1}{1+\frac{1}{4}\omega_0^2+\frac{1}{64}\Delta^2}\left(\mathbf{F}^n+\frac{1}{2}\mathbf{K}\right)\\ &\frac{\frac{1}{64}\Delta^2-\frac{1}{16}\gamma^2}{\left(1+\frac{1}{4}\omega_0^2+\frac{1}{64}\Delta^2\right)\left(1+\frac{1}{4}\omega_0^2+\frac{1}{16}\gamma^2\right)}\mathbf{bb}\cdot\left(\mathbf{F}^n+\frac{1}{2}\mathbf{K}\right)\\ &+\frac{\frac{1}{8}\delta}{\left(1+\frac{1}{4}\omega_0^2+\frac{1}{64}\Delta^2\right)\left(1+\frac{1}{4}\omega_0^2\right)}\mathbf{b}\times\left(\mathbf{F}^n+\frac{1}{2}\mathbf{K}\right).\end{aligned} \tag{D.10}$$

Here, we use the following notations modified from Eqn. (11) of Ref. [25]:

$$\begin{aligned}&\omega_0^2\equiv\sum_s\frac{\omega_s^2\Delta t^2}{1+\Omega_s^2\Delta t^2/4},\\ &\gamma^2=\sum_s\frac{\omega_s^2\Omega_s^2\Delta t^4}{1+\Omega_s^2\Delta t^2/4},\ \delta=\sum_s\frac{\omega_s^2\Omega_s\Delta t^3}{1+\Omega_s^2\Delta t^2/4},\\ &\Delta\equiv\frac{\delta^2}{1+\omega_0^2}.\end{aligned} \tag{D.11}$$

This result is consistent with Eqn. (13) of Ref. [25] though the latter missed a few terms.

In the actual implementation, Eqn. (D.10) is computed first to get $\bar{\mathbf{E}}$, which is substituted in Eqn. (D.6) to compute $\bar{\mathbf{J}}_s$ for each species. The final updated currents and electric fields are then determined by $\mathbf{J}_s^{n+1}=2\bar{\mathbf{J}}_s-\mathbf{J}_s^n$ and $\mathbf{E}^{n+1}=2\bar{\mathbf{E}}-\mathbf{E}^n$. In an informal two-fluid five-moment test, the exact source solution described here is approximately 5× times faster than the solution through matrix inversion using external numerical package.

Appendix E. Stability of the locally implicit scheme

E.1. Von Neumann stability analysis

Following the Von Neumann analysis, we assume all quantities depend on time as $e^{i\omega t}$:

$$\mathbf{q}_s^{n+1}=\mathbf{q}_s^n e^{i\omega\Delta t},\quad \mathbf{q}=[\mathbf{E};\mathbf{J}_s]^T. \tag{E.1}$$

The time-centered quantities are

$$\bar{\mathbf{q}}_s=\frac{\mathbf{q}_s^{n+1}+\mathbf{q}_s^n}{2}=\mathbf{q}_s^n\frac{1+e^{i\omega\Delta t}}{2}. \tag{E.2}$$

For simplicity, we consider the normalized quantities $\tilde{\mathbf{E}}$ and $\tilde{\mathbf{J}}_s$ as defined in Appendix B in this derivation.

First, considering only the plasma oscillation, i.e., neglecting the cyclotron term $\mathbf{J}_s\times\mathbf{\Omega}_s$, the locally implicit scheme gives

$$\begin{cases}\tilde{\bar{\mathbf{E}}} &= \tilde{\mathbf{E}}^n-\frac{\Delta t}{2}\omega_{ps}\sum_s\tilde{\bar{\mathbf{J}}}_s\\ \tilde{\bar{\mathbf{J}}}_s &= \tilde{\mathbf{J}}_s^n+\frac{\Delta t\omega_s}{2}\tilde{\bar{\mathbf{E}}}\end{cases} \tag{E.3}$$

or

$$\mathbf{q}^n\frac{1+e^{i\omega\Delta t}}{2}=\mathbf{q}^n+\frac{\Delta t}{2}\mathbf{M}_\parallel\mathbf{q}^n\frac{1+e^{i\omega\Delta t}}{2}, \tag{E.4}$$

where $\mathbf{q}=\left[\tilde{\mathbf{E}};\tilde{\mathbf{J}}_s\right]^T$ and the coefficient matrix is defined in Eqn. (B.7). Eqn. (E.4) can be rearranged to get

$$\mathbf{q}^n\frac{e^{i\omega\Delta t}-1}{2}=\frac{\Delta t}{2}\mathbf{M}_\parallel\mathbf{q}^n\frac{e^{i\omega\Delta t}+1}{2} \tag{E.5}$$

or

$$\mathbf{q}^n i\tan\left(\frac{\omega\Delta t}{2}\right)=\frac{\Delta t}{2}\mathbf{M}_\parallel\mathbf{q}^n. \tag{E.6}$$

Here, we used the relation

$$1-e^{-i\theta}=2i\sin\frac{\theta}{2}e^{-i\theta/2}\quad\text{and}\quad 1+e^{-i\theta}=2\cos\frac{\theta}{2}e^{-i\theta/2}. \tag{E.7}$$

Recall that $\mathbf{M}_{\parallel}$ has nonzero eigenvalues $\pm i\omega_p$, therefore Eqn. (E.6) gives the stability criterion for plasma oscillation

$$\left(\frac{2}{\Delta t}\right)^2 \tan^2\left(\frac{\omega\Delta t}{2}\right) = \omega_p^2. \tag{E.8}$$

This equation has only real solutions for ω thus eliminates the possibility of numerical instability.

Similarly, we may compute the stability criteria for the perpendicular problem. The results will be of the form

$$\left(\frac{2}{\Delta t}\right)^2 \tan^2\left(\frac{\omega\Delta t}{2}\right) = \omega_\perp^2 \tag{E.9}$$

where $i\omega_\perp$ is an eigenvalue of the matrix $\mathbf{M}_\perp$ defined in Eqn. (B.12). Again, the time-step is not restricted by $\omega_\perp$, which contains both plasma and cyclotron frequencies.

E.2. Properties of the implicit midpoint method

The locally implicit scheme is essentially an implicit midpoint method. Thus it is useful to understand the general properties of the method. Consider the initial value problem of an ODE,

$$y'(t) = f(t, y(t)), \quad y(t_0) = y_0.$$

The implicit midpoint method is given by

$$y_{n+1} = y_n + hf\left(t_n + \frac{h}{2}, \frac{y_n + y_{n+1}}{2}\right). \tag{E.10}$$

It can be written as an implicit Runge-Kutta method

$$\begin{aligned} k &= f\left(t_n + \frac{h}{2}, y_n + \frac{h}{2}k\right) \\ y_{n+1} &= y_n + hk \end{aligned} \tag{E.11}$$

which contains the implicit Euler method with step size $h/2$ as its first part. We may also write the method as

$$\begin{aligned} \bar{y} &= y_n + \frac{h}{2} f\left(t_n + \frac{h}{2}, \bar{y}\right) \\ y_{n+1} &= y_n + hf\left(t_n + \frac{h}{2}, \bar{y}\right) \end{aligned} \tag{E.12}$$

since

$$y_{n+1} - 2\bar{y} = y_n - 2y_n = -y_n \Leftrightarrow \bar{y} = \frac{y_n + y_{n+1}}{2}. \tag{E.13}$$

An additional observation is that the second step in Eqn. (E.12) can then be replaced by $y_{n+1} = 2\bar{y} - y_n$. This simplifies the implementation and is used in our code.

The implicit midpoint method has local truncation error of order $O\left(h^3\right)$ hence global error of order $O\left(h^2\right)$. As shown in the von Neumann stability diagram Fig. 6, for a problem $y = e^{\lambda t}$, the stability region of the method is the entire half plane with $Im(\lambda)h \leq 0$, thus the method is unconditionally stable for nongrowing problems. For an purely oscillatory problem, like our source update equations, λ lies right on the border of the stability region (the imaginary axis), indicating exact preservation of oscillation magnitude.

Appendix F. The eigensystem of the ten-moment model

To determine the eigensystem of the homogeneous part of the ten-moment equations we first write, in one-dimension, the left-hand side of Eqns. (1), (2) and (12), in the quasilinear form

$$\partial_t \mathbf{v} + \mathbf{A}\partial_1 \mathbf{v} = 0 \tag{F.1}$$

where $\mathbf{v}$ is the vector of primitive variables and $\mathbf{A}$ is a matrix of coefficients. For the ten-moment system we have

$$\mathbf{v} = \left[\rho, u_1, u_2, u_3, P_{11}, P_{12}, P_{13}, P_{22}, P_{23}, P_{33}\right]^T \tag{F.2}$$

where $\rho \equiv mn$ and

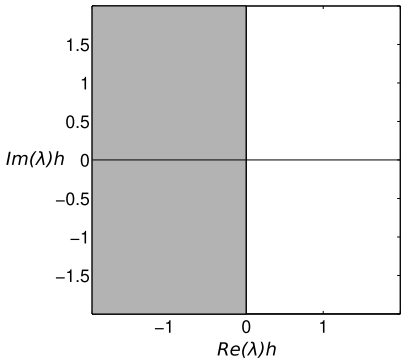

Fig. 6. The gray shadows represent the stability region of the implicit midpoint method on the complex plane. A purely oscillatory problem lies on the imaginary axis, which is exactly the boundary of the stability region. Therefore, when applied to a purely oscillatory problem, the locally midpoint method conserves the amplitude, i.e., no damping or amplifying.

$$\mathbf{A}=\begin{bmatrix} u_1 & \rho & 0 & 0 & 0 & 0 & 0 & 0 & 0 & 0 \\ 0 & u_1 & 0 & 0 & 1/\rho & 0 & 0 & 0 & 0 & 0 \\ 0 & 0 & u_1 & 0 & 0 & 1/\rho & 0 & 0 & 0 & 0 \\ 0 & 0 & 0 & u_1 & 0 & 0 & 1/\rho & 0 & 0 & 0 \\ 0 & 3P_{11} & 0 & 0 & u_1 & 0 & 0 & 0 & 0 & 0 \\ 0 & 2P_{12} & P_{11} & 0 & 0 & u_1 & 0 & 0 & 0 & 0 \\ 0 & 2P_{13} & 0 & P_{11} & 0 & 0 & u_1 & 0 & 0 & 0 \\ 0 & P_{22} & 2P_{12} & 0 & 0 & 0 & 0 & u_1 & 0 & 0 \\ 0 & P_{23} & P_{13} & P_{12} & 0 & 0 & 0 & 0 & u_1 & 0 \\ 0 & P_{33} & 0 & 2P_{13} & 0 & 0 & 0 & 0 & 0 & u_1 \end{bmatrix} \tag{F.3}$$

The eigensystem of this matrix can be easily obtained either by hand or a computer algebra package. The results are described below.

The eigenvalues of the system are given by

$$\lambda^{1,2}=u_1-\sqrt{P_{11}/\rho} \tag{F.4}$$

$$\lambda^{3,4}=u_1+\sqrt{P_{11}/\rho} \tag{F.5}$$

$$\lambda^{5}=u_1-\sqrt{3P_{11}/\rho} \tag{F.6}$$

$$\lambda^{6}=u_1+\sqrt{3P_{11}/\rho} \tag{F.7}$$

$$\lambda^{7,8,9,10}=u_1 \tag{F.8}$$

To maintain hyperbolicity we must hence have $\rho>0$ and $P_{11}>0$. In multiple dimensions, in general, the diagonal elements of the pressure tensor must be positive. When $P_{11}=0$ the system reduces to the cold fluid equations which is known to be rank deficient and hence not hyperbolic as usually understood.[2] Also notice that the eigenvalues do not include the usual fluid sound-speed $c_s=\sqrt{5p/3\rho}$ but instead have two different propagation speeds $c_1=\sqrt{P_{11}/\rho}$ and $c_2=\sqrt{3P_{11}/\rho}$. This is because the (neutral) ten-moment system does not go to the correct limit of Euler equations in the absence of collisions. In fact, it is collisions that drive the pressure tensor to isotropy, but do not appear in the homogeneous ten-moment system.

The right eigenvectors (column vectors) are given below.

$$\mathbf{r}^{1,3}=\begin{bmatrix} 0 \\ 0 \\ \mp c_1 \\ 0 \\ 0 \\ P_{11} \\ 0 \\ 2P_{12} \\ P_{13} \\ 0 \end{bmatrix} \quad \mathbf{r}^{2,4}=\begin{bmatrix} 0 \\ 0 \\ 0 \\ \mp c_1 \\ 0 \\ 0 \\ P_{11} \\ 0 \\ P_{12} \\ 2P_{13} \end{bmatrix} \tag{F.9}$$

[2] For hyperbolicity the matrix A must posses real eigenvalues and a complete set of linearly independent right eigenvectors. For the cold fluid system we only have a single eigenvalue (the fluid velocity) and a single eigenvector. This can lead to generalized solutions like delta shocks.

and

$$\mathbf{r}^{5,6} = \begin{bmatrix} \rho P_{11} \\ \mp c_2 P_{11} \\ \mp c_2 P_{12} \\ \mp c_2 P_{13} \\ 3P_{11}^2 \\ 3P_{11}P_{12} \\ 3P_{11}P_{13} \\ P_{11}P_{22} + 2P_{12}^2 \\ P_{11}P_{23} + 2P_{12}P_{13} \\ P_{11}P_{33} + 2P_{13}^2 \end{bmatrix} \tag{F.10}$$

and

$$\mathbf{r}^7 = \begin{bmatrix} 1 \\ 0 \\ 0 \\ 0 \\ 0 \\ 0 \\ 0 \\ 0 \\ 0 \\ 0 \end{bmatrix} \quad \mathbf{r}^8 = \begin{bmatrix} 0 \\ 0 \\ 0 \\ 0 \\ 0 \\ 0 \\ 0 \\ 1 \\ 0 \\ 0 \end{bmatrix} \quad \mathbf{r}^9 = \begin{bmatrix} 0 \\ 0 \\ 0 \\ 0 \\ 0 \\ 0 \\ 0 \\ 0 \\ 1 \\ 0 \end{bmatrix} \quad \mathbf{r}^{10} = \begin{bmatrix} 0 \\ 0 \\ 0 \\ 0 \\ 0 \\ 0 \\ 0 \\ 0 \\ 0 \\ 1 \end{bmatrix} \tag{F.11}$$

We can now compute the left eigenvectors (row vectors) by inverting the matrix with right eigenvectors stored as columns. This ensures the normalization $\mathbf{l}^p \mathbf{r}^k = \delta^{pk}$, where the $\mathbf{l}^p$ are the left eigenvectors. On performing the inversion we have

$$\mathbf{l}^{1,3} = \begin{bmatrix} 0 & \pm\dfrac{P_{12}}{2c_1 P_{11}} & \mp\dfrac{1}{2c_1} & 0 & -\dfrac{P_{12}}{2P_{11}^2} & \dfrac{1}{2P_{11}} & 0 & 0 & 0 & 0 \end{bmatrix} \tag{F.12}$$

$$\mathbf{l}^{2,4} = \begin{bmatrix} 0 & \pm\dfrac{P_{13}}{2c_1 P_{11}} & 0 & \mp\dfrac{1}{2c_1} & -\dfrac{P_{13}}{2P_{11}^2} & 0 & \dfrac{1}{2P_{11}} & 0 & 0 & 0 \end{bmatrix} \tag{F.13}$$

and

$$\mathbf{l}^{5,6} = \begin{bmatrix} 0 & \mp\dfrac{1}{2c_2 P_{11}} & 0 & 0 & \dfrac{1}{6P_{11}^2} & 0 & 0 & 0 & 0 & 0 \end{bmatrix} \tag{F.14}$$

and

$$\mathbf{l}^7 = \begin{bmatrix} 1 & 0 & 0 & 0 & -\dfrac{1}{3c_1^2} & 0 & 0 & 0 & 0 & 0 \end{bmatrix} \tag{F.15}$$

$$\mathbf{l}^8 = \begin{bmatrix} 0 & 0 & 0 & 0 & \dfrac{4P_{12}^2 - P_{11}P_{22}}{3P_{11}^2} & -\dfrac{2P_{12}}{P_{11}} & 0 & 1 & 0 & 0 \end{bmatrix} \tag{F.16}$$

$$\mathbf{l}^9 = \begin{bmatrix} 0 & 0 & 0 & 0 & \dfrac{4P_{12}P_{13} - P_{11}P_{23}}{3P_{11}^2} & -\dfrac{P_{13}}{P_{11}} & -\dfrac{P_{12}}{P_{11}} & 0 & 1 & 0 \end{bmatrix} \tag{F.17}$$

$$\mathbf{l}^{10} = \begin{bmatrix} 0 & 0 & 0 & 0 & \dfrac{4P_{13}^2 - P_{11}P_{33}}{3P_{11}^2} & 0 & -\dfrac{2P_{13}}{P_{11}} & 0 & 0 & 1 \end{bmatrix} \tag{F.18}$$

Most often, for numerical simulations, the eigensystem of the conservation form of the homogeneous system is needed. This eigensystem is related to the eigensystem of the quasilinear form derived above. To see this consider a conservation law

$$\partial_t \mathbf{q} + \partial_1 \mathbf{f} = 0 \tag{F.19}$$

where $\mathbf{f} = \mathbf{f}(\mathbf{q})$ is a flux function. Now consider an invertible transformation $\mathbf{q} = \varphi(\mathbf{v})$. This transforms the conservation law to

$$\partial_t \mathbf{v} + (\varphi')^{-1} \, D\mathbf{f} \, \varphi' \partial_1 \mathbf{v} = 0 \tag{F.20}$$

where φ' is the Jacobian matrix of the transformation and $D\mathbf{f} \equiv \partial \mathbf{f}/\partial \mathbf{q}$ is the flux Jacobian. Comparing this to Eqn. (F.1) we see that the quasilinear matrix is related to the flux Jacobian by

$$\mathbf{A} = (\varphi')^{-1}\, D\mathbf{f}\, \varphi' \tag{F.21}$$

This clearly shows that the eigenvalues of the flux Jacobian are the same as those of the quasilinear matrix while the right and left eigenvectors can be computed using $\varphi'\mathbf{r}^p$ and $\mathbf{l}^p(\varphi')^{-1}$ respectively.

For the ten-moment system the required transformation is

$$\mathbf{q} = \varphi(\mathbf{v}) = \begin{bmatrix} \rho \\ \rho u_1 \\ \rho u_2 \\ \rho u_3 \\ \rho u_1 u_1 + P_{11} \\ \rho u_1 u_2 + P_{12} \\ \rho u_1 u_3 + P_{13} \\ \rho u_2 u_2 + P_{22} \\ \rho u_2 u_3 + P_{23} \\ \rho u_3 u_3 + P_{33} \end{bmatrix} \tag{F.22}$$

For this transformation we have

$$\varphi'(\mathbf{v}) = \begin{bmatrix} 1 & 0 & 0 & 0 & 0 & 0 & 0 & 0 & 0 & 0 \\ u_1 & \rho & 0 & 0 & 0 & 0 & 0 & 0 & 0 & 0 \\ u_2 & 0 & \rho & 0 & 0 & 0 & 0 & 0 & 0 & 0 \\ u_3 & 0 & 0 & \rho & 0 & 0 & 0 & 0 & 0 & 0 \\ u_1 u_1 & 2\rho u_1 & 0 & 0 & 1 & 0 & 0 & 0 & 0 & 0 \\ u_1 u_2 & \rho u_2 & \rho u_1 & 0 & 0 & 1 & 0 & 0 & 0 & 0 \\ u_1 u_3 & \rho u_3 & 0 & \rho u_1 & 0 & 0 & 1 & 0 & 0 & 0 \\ u_2 u_2 & 0 & 2\rho u_2 & 0 & 0 & 0 & 0 & 1 & 0 & 0 \\ u_2 u_3 & 0 & \rho u_3 & \rho u_2 & 0 & 0 & 0 & 0 & 1 & 0 \\ u_3 u_3 & 0 & 0 & 2\rho u_3 & 0 & 0 & 0 & 0 & 0 & 1 \end{bmatrix} \tag{F.23}$$

The inverse of the transformation Jacobian is

$$(\varphi')^{-1} = \begin{bmatrix} 1 & 0 & 0 & 0 & 0 & 0 & 0 & 0 & 0 & 0 \\ -u_1/\rho & 1/\rho & 0 & 0 & 0 & 0 & 0 & 0 & 0 & 0 \\ -u_2/\rho & 0 & 1/\rho & 0 & 0 & 0 & 0 & 0 & 0 & 0 \\ -u_3/\rho & 0 & 0 & 1/\rho & 0 & 0 & 0 & 0 & 0 & 0 \\ u_1 u_1 & -2u_1 & 0 & 0 & 1 & 0 & 0 & 0 & 0 & 0 \\ u_1 u_2 & -u_2 & -u_1 & 0 & 0 & 1 & 0 & 0 & 0 & 0 \\ u_1 u_3 & -u_3 & 0 & -u_1 & 0 & 0 & 1 & 0 & 0 & 0 \\ u_2 u_2 & 0 & -2u_2 & 0 & 0 & 0 & 0 & 1 & 0 & 0 \\ u_2 u_3 & 0 & -u_3 & -u_2 & 0 & 0 & 0 & 0 & 1 & 0 \\ u_3 u_3 & 0 & 0 & -2u_3 & 0 & 0 & 0 & 0 & 0 & 1 \end{bmatrix} \tag{F.24}$$

References

[1] A. Hakim, J. Loverich, U. Shumlak, A high resolution wave propagation scheme for ideal two-fluid plasma equations, J. Comput. Phys. 219 (2006) 418–442, https://doi.org/10.1016/j.jcp.2006.03.036, http://www.sciencedirect.com/science/article/pii/S0021999106001707.

[2] A.H. Hakim, Extended MHD modelling with the ten-moment equations, J. Fusion Energy 27 (2008) 36–43, https://doi.org/10.1007/s10894-007-9116-z, http://link.springer.com/article/10.1007/s10894-007-9116-z.

[3] E.A. Johnson, Gaussian-moment relaxation closures for verifiable numerical simulation of fast magnetic reconnection in plasma, preprint, arXiv:1409.6985, 2014.

[4] L. Wang, A.H.A. Hakim, A. Bhattacharjee, K. Germaschewski, Comparison of multi-fluid moment models with particle-in-cell simulations of collisionless magnetic reconnection, Phys. Plasmas 22 (1) (2015) 012108, https://doi.org/10.1063/1.4906063, http://scitation.aip.org/content/aip/journal/pop/22/1/10.1063/1.4906063.

[5] J. Ng, A. Hakim, A. Bhattacharjee, A. Stanier, W. Daughton, Simulations of anti-parallel reconnection using a nonlocal heat flux closure, Phys. Plasmas 24 (8) (2017) 082112, https://doi.org/10.1063/1.4993195, http://aip.scitation.org/doi/10.1063/1.4993195.

[6] J. Ng, A. Hakim, A. Bhattacharjee, A twenty-moment model for collisionless guide field reconnection, in: APS Division of Plasma Physics Meeting 2015, 2015, abstract id. NP12.100, http://adsabs.harvard.edu/abs/2015APS..DPPN12100N.

[7] R.M. Kulsrud, Mhd description of plasma, in: Handbook of Plasma Physics, vol. 1, 1983, p. 115.

[8] B. Srinivasan, U. Shumlak, Analytical and computational study of the ideal full two-fluid plasma model and asymptotic approximations for Hall-magnetohydrodynamics, Phys. Plasmas 18 (9) (2011) 092113, https://doi.org/10.1063/1.3640811, http://aip.scitation.org/doi/10.1063/1.3640811.

[9] J.W. Burby, Magnetohydrodynamic motion of a two-fluid plasma, Phys. Plasmas 24 (8) (2017), https://doi.org/10.1063/1.4994068, arXiv:1705.02654.

[10] G.W. Hammett, F.W. Perkins, Fluid moment models for Landau damping with application to the ion-temperature-gradient instability, Phys. Rev. Lett. 64 (25) (1990) 3019–3022, https://doi.org/10.1103/PhysRevLett.64.3019, http://link.aps.org/doi/10.1103/PhysRevLett.64.3019.

[11] F. Allmann-Rahn, T. Trost, R. Grauer, Temperature gradient driven heat flux closure in fluid simulations of collisionless reconnection, J. Plasma Phys. 84 (03) (2018) 905840307, https://doi.org/10.1017/S002237781800048X, https://www.cambridge.org/core/product/identifier/S002237781800048X/type/journal_article.

[12] P. Hunana, G. Zank, M. Laurenza, A. Tenerani, G. Webb, M. Goldstein, M. Velli, L. Adhikari, New closures for more precise modeling of Landau damping in the fluid framework, Phys. Rev. Lett. 121 (13) (2018) 135101.

[13] C.K. Birdsall, A.B. Langdon, Plasma Physics via Computer Simulation, McGraw-Hill, 1985, http://adsabs.harvard.edu/abs/1991ppcs.book.....B.

[14] G. Strang, On the construction and comparison of difference schemes, SIAM J. Numer. Anal. 5 (3) (1968) 506–517, https://doi.org/10.1137/0705041, http://epubs.siam.org/doi/abs/10.1137/0705041.

[15] R.J. LeVeque, Finite Volume Methods for Hyperbolic Problems, Cambridge University Press, Cambridge, 2002, http://ebooks.cambridge.org/ref/id/CBO9780511791253.

[16] A.G. Kulikoviskii, N.V. Pogorelov, A.Y. Semenov, Mathematical Aspects of Numerical Solutions of Hyperbolic Systems, Chapman and Hall/CRC, 2001.

[17] B. Cockburn, C.W. Shu, Runge–Kutta discontinuous Galerkin methods for convection-dominated problems, J. Sci. Comput. 16 (3) (2001) 173–261.

[18] J.S. Hesthaven, T. Warburton, Nodal Discontinuous Galerkin Methods: Algorithms, Analysis and Applications, Springer, 2008.

[19] J. Loverich, A. Hakim, U. Shumlak, A discontinuous Galerkin method for ideal two-fluid plasma equations, Commun. Comput. Phys. (2010).

[20] H. Kumar, S. Mishra, Entropy stable numerical schemes for two-fluid plasma equations, J. Sci. Comput. 52 (2) (2012) 401–425, https://doi.org/10.1007/s10915-011-9554-7, http://link.springer.com/10.1007/s10915-011-9554-7.

[21] R. Abgrall, H. Kumar, Robust finite volume schemes for two-fluid plasma equations, J. Sci. Comput. 60 (3) (2014) 584–611, https://doi.org/10.1007/s10915-013-9809-6, http://link.springer.com/10.1007/s10915-013-9809-6.

[22] D.S. Balsara, T. Amano, S. Garain, J. Kim, A high-order relativistic two-fluid electrodynamic scheme with consistent reconstruction of electromagnetic fields and a multidimensional Riemann solver for electromagnetism, J. Comput. Phys. 318 (2016) 169–200, https://doi.org/10.1016/j.jcp.2016.05.006, arXiv:1603.06975.

[23] Z. Huang, G. Tóth, B. van der Holst, Y. Chen, T. Gombosi, A six-moment multi-fluid plasma model, J. Comput. Phys. 387 (2019) 134–153.

[24] U. Shumlak, J. Loverich, Approximate Riemann solver for the two-fluid plasma model, J. Comput. Phys. 187 (2) (2003) 620–638, https://doi.org/10.1016/S0021-9991(03)00151-7, http://linkinghub.elsevier.com/retrieve/pii/S0021999103001517.

[25] D.N. Smithe, Finite-difference time-domain simulation of fusion plasmas at radiofrequency time scales, Phys. Plasmas 14 (5) (2007) 056104, https://doi.org/10.1063/1.2710784, http://scitation.aip.org/content/aip/journal/pop/14/5/10.1063/1.2710784.

[26] J.B. Et, et al., Geospace environmental modeling ({GEM}) magnetic reconnection challenge, J. Geophys. Res. 106 (2001) 3715.

[27] J.M. TenBarge, J. Ng, J. Juno, L. Wang, A.H. Hakim, A. Bhattacharjee, An extended MHD study of the 16 October 2015 MMS diffusion region crossing, J. Geophys. Res. Space Phys. 124 (11) (2019) 8474–8487, https://doi.org/10.1029/2019ja026731.

[28] S.A. Orszag, C.-M. Tang, Small-scale structure of two-dimensional magnetohydrodynamic turbulence, J. Fluid Mech. 90 (01) (1979) 129, https://doi.org/10.1017/S002211207900210X, http://www.journals.cambridge.org/abstract_S002211207900210X.

[29] G. Tóth, The divB=0 constraint in shock-capturing magnetohydrodynamics codes, J. Comput. Phys. 161 (2) (2000) 605–652, https://doi.org/10.1006/jcph.2000.6519, http://linkinghub.elsevier.com/retrieve/pii/S0021999100965197.

[30] J.M. Stone, T.A. Gardiner, P. Teuben, J.F. Hawley, J.B. Simon, Athena: a new code for astrophysical MHD, Astrophys. J. Suppl. Ser. 178 (1) (2008) 137–177, https://doi.org/10.1086/588755, http://stacks.iop.org/0067-0049/178/i=1/a=137.

[31] B. Dudson, M. Umansky, X. Xu, P. Snyder, H. Wilson, BOUT++: a framework for parallel plasma fluid simulations, Comput. Phys. Commun. 180 (9) (2009) 1467–1480, https://doi.org/10.1016/j.cpc.2009.03.008, http://linkinghub.elsevier.com/retrieve/pii/S0010465509001040.

[32] L. Wang, K. Germaschewski, A. Hakim, C. Dong, J. Raeder, A. Bhattacharjee, Electron physics in 3-d two-fluid 10-moment modeling of Ganymede's magnetosphere, J. Geophys. Res. Space Phys. 123 (4) (2018) 2815–2830, https://doi.org/10.1002/2017ja024761.

[33] C. Dong, L. Wang, A. Hakim, A. Bhattacharjee, J.A. Slavin, G.A. DiBraccio, K. Germaschewski, Global ten-moment multifluid simulations of the solar wind interaction with mercury: from the planetary conducting core to the dynamic magnetosphere, Geophys. Res. Lett. 46 (21) (2019) 11584–11596, https://doi.org/10.1029/2019gl083180.

[34] J. Ng, Y.-M. Huang, A. Hakim, A. Bhattacharjee, A. Stanier, W. Daughton, L. Wang, K. Germaschewski, The island coalescence problem: scaling of reconnection in extended fluid models including higher-order moments, Phys. Plasmas 22 (11) (2015) 112104, https://doi.org/10.1063/1.4935302, http://scitation.aip.org/content/aip/journal/pop/22/11/10.1063/1.4935302.

[35] T. Amano, Divergence-free approximate Riemann solver for the quasi-neutral two-fluid plasma model, J. Comput. Phys. 299 (2015) 863–886, https://doi.org/10.1016/j.jcp.2015.07.035, arXiv:1507.06022.

[36] K. Hirabayashi, M. Hoshino, T. Amano, A new framework for magnetohydrodynamic simulations with anisotropic pressure, J. Comput. Phys. 327 (2016) 851–872, https://doi.org/10.1016/j.jcp.2016.09.064, arXiv:1606.07982.

[37] S. Zenitani, M. Hesse, A. Klimas, Relativistic two-fluid simulations of guide field magnetic reconnection, Astrophys. J. 705 (1) (2009) 907–913, https://doi.org/10.1088/0004-637X/705/1/907, http://stacks.iop.org/0004-637X/705/i=1/a=907?key=crossref.4edeb4038a0207dcf0f22b1546162dbd.

[38] S. Lautenbach, R. Grauer, Multiphysics simulations of collisionless plasmas, Front. Phys. 6 (2018) 113, https://doi.org/10.3389/fphy.2018.00113, https://www.frontiersin.org/article/10.3389/fphy.2018.00113/full.

[39] V. Joncquieres, F. Pechereau, A. Alvarez Laguna, A. Bourdon, O. Vermorel, B. Cuenot, A 10-moment fluid numerical solver of plasma with sheaths in a hall effect thruster, in: 2018 Joint Propulsion Conference, 2018, p. 4905.

[40] A.A. Laguna, A. Lani, N.N. Mansour, H. Deconinck, S. Poedts, Effect of radiation on chromospheric magnetic reconnection: reactive and collisional multi-fluid simulations, Astrophys. J. 842 (2) (2017) 117.

[41] A. Alvarez-Laguna, N. Ozak, A. Lani, N. Mansour, H. Deconinck, S. Poedts, A versatile numerical method for the multi-fluid plasma model in partially- and fully-ionized plasmas, J. Phys. Conf. Ser. 1031 (2018) 012015, IOP Publishing.

[42] A.A. Laguna, N. Ozak, A. Lani, H. Deconinck, S. Poedts, Fully-implicit finite volume method for the ideal two-fluid plasma model, Comput. Phys. Commun. 231 (2018) 31–44.

[43] S. Jarmak, E. Leonard, A. Akins, E. Dahl, D. Cremons, S. Cofield, A. Curtis, C. Dong, E. Dunham, B. Journaux, D. Murakami, W. Ng, M. Piquette, A.P. Girija, K. Rink, L. Schurmeier, N. Stein, N. Tallarida, M. Telus, L. Lowes, C. Budney, K. Mitchell, Quest: a new frontiers Uranus orbiter mission concept study, Acta Astronaut. 170 (2020) 6–26, https://doi.org/10.1016/j.actaastro.2020.01.030, http://www.sciencedirect.com/science/article/pii/S0094576520300412.

[44] J. Ng, A. Hakim, J. Juno, A. Bhattacharjee, Drift instabilities in thin current sheets using a two-fluid model with pressure tensor effects, J. Geophys. Res. Space Phys. 124 (5) (2019) 3331–3346, https://doi.org/10.1029/2018JA026313, https://agupubs.onlinelibrary.wiley.com/doi/abs/10.1029/2018JA026313.

[45] P. Cagas, A. Hakim, J. Juno, B. Srinivasan, Continuum kinetic and multi-fluid simulations of classical sheaths, Phys. Plasmas 24 (2) (2017) 022118, https://doi.org/10.1063/1.4976544, http://aip.scitation.org/doi/10.1063/1.4976544.
[46] J. Ng, A. Hakim, A. Bhattacharjee, Using the maximum entropy distribution to describe electrons in reconnecting current sheets, Phys. Plasmas 25 (8) (2018) 082113, https://doi.org/10.1063/1.5041758, http://aip.scitation.org/doi/10.1063/1.5041758.
[47] L. Chacón, D.A. Knoll, A 2D high-β Hall MHD implicit nonlinear solver, J. Comput. Phys. 188 (2) (2003) 573–592.
[48] G. Tóth, Y. Ma, T.I. Gombosi, Hall magnetohydrodynamics on block-adaptive grids, J. Comput. Phys. 227 (14) (2008) 6967–6984.
[49] P. Degond, F. Deluzet, D. Doyen, Asymptotic-preserving particle-in-cell methods for the Vlasov–Maxwell system in the quasi-neutral limit, J. Comput. Phys. 330 (2017) 467–492, https://doi.org/10.1016/j.jcp.2016.11.018.